The Astrophysical Journal Letters, 990:L8 (24pp), 2025 September 1 https://doi.org/10.3847/2041-8213/adf721

WIde Separation Planets In Time (WISPIT): A Gap-clearing Planet in a Multi-ringed Disk around the Young Solar-type Star WISPIT 2

Richelle F. van Capelleveen[1], Christian Ginski[2], Matthew A. Kenworthy[1], Jake Byrne[2], Chloe Lawlor[2], Dan McLachlan[2], Eric E. Mamajek[3], Tomas Stolker[1], Myriam Benisty[4], Alexander J. Bohn[1], Laird M. Close[5], Carsten Dominik[6], Sebastiaan Haffert[1,5], Rico Landman[1], Jie Ma[7], Ignas Snellen[1], Ryo Tazaki[8], Nienke van der Marel[1], Lukas Welzel[1], and Yapeng Zhang[9]

[1] Leiden Observatory, Leiden University, Postbus 9513, 2300 RA Leiden, The Netherlands; capelleveen@strw.leidenuniv.nl
[2] School of Natural Sciences, Center for Astronomy, University of Galway, Galway, H91 CF50, Ireland
[3] Jet Propulsion Laboratory, California Institute of Technology, 4800 Oak Grove Drive, M/S 321-162, Pasadena, CA 91109, USA
[4] Max-Planck-Institut für Astronomie, Königstuhl 17, 69117 Heidelberg, Germany
[5] Steward Observatory, University of Arizona, 933 N. Cherry Avenue, Tucson, AZ 85719, USA
[6] Anton Pannekoek Institute for Astronomy, University of Amsterdam, Science Park 904, 1098 XH Amsterdam, The Netherlands
[7] Université Grenoble Alpes, CNRS, Institut de Planétologie et d'Astrophysique (IPAG), F-38000, France
[8] Department of Earth Science and Astronomy, The University of Tokyo, Tokyo 153-8902, Japan
[9] Department of Astronomy, California Institute of Technology, Pasadena, CA 91125, USA

Received 2025 July 3; revised 2025 July 28; accepted 2025 August 2; published 2025 August 26

Abstract

In the past decades, several thousand exoplanet systems have been discovered around evolved, main-sequence stars, revealing a wide diversity in their architectures. To understand how the planet formation process can lead to vastly different outcomes in system architecture, we have to study the starting conditions of planet formation within the disks around young stars. In this study, we are presenting high-resolution direct imaging observations with the Very Large Telescope/SPHERE of the young (∼5 Myr), nearby (∼133 pc), solar-analog designated as WISPIT 2 (= TYC 5709-354-1). These observations were taken as part of our survey program that explores the formation and orbital evolution of wide-separation gas giants. WISPIT 2 was observed in four independent epochs using polarized light and total intensity observations. They reveal for the first time an extended (380 au) disk in scattered light with a multi-ringed substructure. We directly detect a young protoplanet, WISPIT 2b, embedded in a disk gap and show that it is comoving with its host star. Multiple SPHERE epochs demonstrate that it shows orbital motion consistent with Keplerian motion in the observed disk gap. Our H- and K_s-band photometric data are consistent with thermal emission from a young planet. By comparison with planet evolutionary models, we find a mass of the planet of $4.9^{+0.9}_{-0.6} M_{\rm Jup}$. This mass is also consistent with the width of the observed disk gap, retrieved from hydrodynamic models. WISPIT 2b is the first unambiguous planet detection in a multi-ringed disk, making the WISPIT 2 system the ideal laboratory to study planet–disk interaction and subsequent evolution.

Unified Astronomy Thesaurus concepts: Exoplanets (498); Exoplanet formation (492); Circumstellar disks (235); Direct imaging (387); Polarimetry (1278)

1. Introduction

It has only been three decades since the first exoplanet detection, but tremendous progress has been made since: to date, there are nearly 6000 confirmed exoplanets. These planets span a wide range of masses, are found at separations from less than an astronomical unit (e.g., R. I. Dawson & D. C. Fabrycky 2010; E. Goffo et al. 2023) to several hundreds of astronomical units from their host stars (e.g., M. Janson et al. 2021; Z. Zhang et al. 2021), and exhibit diverse atmospheric chemistries (e.g., R. J. MacDonald & N. Madhusudhan 2017; Z. Rustamkulov et al. 2023; C. Gapp et al. 2025), with some planets even hosting circumplanetary disks (CPDs; e.g., M. Benisty et al. 2021; L. M. Close et al. 2025a). They have been found around a variety of stellar types, including stellar multiples (e.g., S. Sigurdsson et al. 2003; T. J. Dupuy et al. 2018; V. B. Kostov et al. 2020), though the majority have been detected around single stars. This diversity raises a fundamental question: are planetary properties inherited from their natal disks, or shaped by later evolutionary processes? Addressing this question requires a detailed understanding of the environments in which planets form—their protoplanetary disks.

As the disk and planet evolve simultaneously, the disk affects the planet and the planet in turn affects the disk. This is evident in the formation of substructures and in the distribution of gas and dust. Combined observations from high-contrast imaging—sensitive to thermal emission and scattered light from (sub)micron-sized dust—and the Atacama Large Millimeter/submillimeter Array (ALMA), which traces gas and millimeter dust, have revealed a wide variety of such substructures. These findings have provided critical inputs for theoretical models of disk dynamical evolution and planet–disk interactions (see review J. Bae et al. 2023, and citations therein).

The next logical step toward advancing our understanding of planet–disk interactions in early planet formation is to test these models against observations of planet-forming disks with embedded protoplanets. This remains challenging, however, as to date, only one system—PDS 70—has been unambiguously confirmed to host embedded protoplanets (M. Keppler et al. 2018; S. Y. Haffert et al. 2019). While several notable candidate systems exist (e.g., R. Gratton et al. 2019; T. Currie et al. 2022), confirmation is hindered by the difficulty of disentangling planet signal from disk signal (e.g., K. B. Follette et al. 2017; T. Currie et al. 2019). In the case of direct detections, the challenge lies in determining whether the detected emission originates from a planet or from disk structures. For indirect methods, such as detections based on kinematic signatures, the difficulty lies in distinguishing between deviations from Keplerian velocity caused by an embedded planet and those resulting from intrinsic disk dynamics in the absence of a planet (R. Teague et al. 2025). These difficulties are compounded by the technical complexity of detecting low-mass planets, especially through accretion signals (M. Benisty et al. 2023; L. M. Close et al. 2025a). This scarcity of testbeds, both in number and diversity, leaves key questions about planet formation unresolved.

One such question concerns the formation of wide-separation giant planets orbiting at semimajor axes larger than 50 au. It remains unclear whether these are formed in situ through gravitational instability, either through interstellar cloud fragmentation or circumstellar disk fragmentation (P. Kroupa 1995; A. P. Boss 1997), or whether they were formed closer to the star through accretion processes (J. B. Pollack et al. 1996) and migrated outward later through scattering events. Along with the broader goal of discovering planets and determining their occurrence rates around stars similar to our Sun, this gave rise to the Young Suns Exoplanet Survey (YSES; A. J. Bohn et al. 2021; R. F. van Capelleveen 2025, in preparation), a Very Large Telescope (VLT)/SPHERE direct imaging survey targeting 70 young (14 ± 3 Myr), solar-mass stars in the Lower Centaurus Crux subgroup of the Scorpius-Centaurus (Sco-Cen) OB association. Building on the success of YSES, the WIde Separation Planets In Time (WISPIT; R. F. van Capelleveen et al. 2025; R. F. van Capelleveen 2025, in preparation) survey extends this sample to younger ages—the median age is 8.5 Myr—and to other regions of the sky. This ongoing survey comprises a total of 178 young suns, making it the closest and largest selection of young solar-mass stars.

The best way to test (wide-separation) planet formation and planet–disk interaction theories is finding unambiguous planet signals embedded in disks around young stars. In this work, we present such a discovery: a robust detection of a planetary companion embedded in a ringed disk around WISPIT 2 (=TYC 5709-354-1)—see Figure 1. In Section 2 we present the stellar properties of WISPIT 2, followed by our observations and data processing in Section 3. In Section 4 we detail the morphology and analysis of the scattered light from the multi-ringed disk. The characterization of multiple epochs of the planet along with its orbital properties are detailed in Section 5, and its subsequent interaction with the disk follows in Section 6. The planetary interpretation of WISPIT 2b is additionally strengthened by its detection in Hα observations (L. M. Close et al. 2025b, companion Letter 2). Our discussion and conclusions are presented in Section 8.

2. Stellar Properties of WISPIT 2

WISPIT 2 was flagged as a pre-main-sequence star candidate by E. Zari et al. (2018), and is fairly proximate ($d = 133.35^{+0.37}_{-0.38}$ pc; C. A. L. Bailer-Jones et al. 2021), which is how it came to be included in the WISPIT survey. Its combined stellar properties are listed in Table 1. WISPIT 2 is located in the outskirts of the Scorpius-Centaurus OB association but has not been assigned membership to any of its main subgroups, and its astrometry is not consistent with membership in any of them. We discuss its comoving codistant stars and membership to recently identified young stellar associations in Appendix A.2, and found that it is likely part of the Theia 53 (M. Kounkel & K. Covey 2019; R. M. P. Kerr et al. 2021; E. L. Hunt & S. Reffert 2024) group. Based on lithium equivalent width measurements of three stars assigned to this group, we used Estimating AGes from Lithium Equivalent widthS (EAGLES) and EAGLES v2.0 to estimate the age of this cluster, resulting in age constraints of <13 Myr and $11.1^{+5.9}_{-8.1}$ Myr, respectively (see Appendix A.3 for more details).

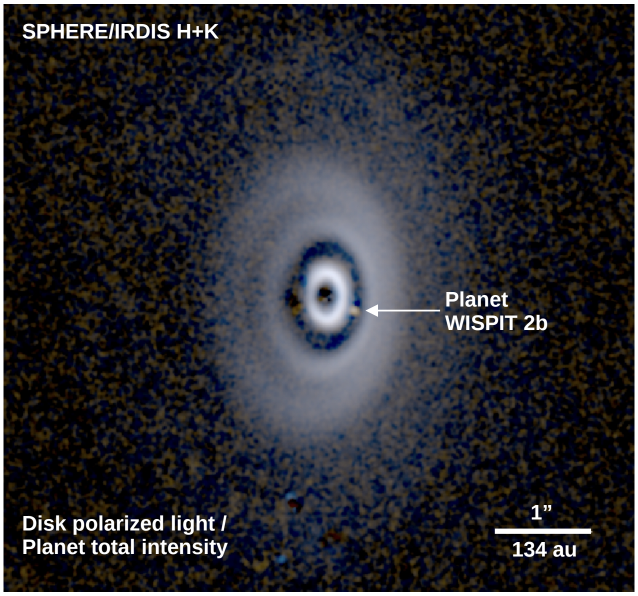

Figure 1. Shown here is a SPHERE/IRDIS multiband image of the WISPIT 2 system. The H-band Q_ϕ image was added as the blue channel and the median combination of H-band and K_s-band Q_ϕ images was added as the green channel. The red channel is a combination of a K_s-band Q_ϕ image and a K_s-band cADI image in which we masked all but the gap containing the thermal emission from WISPIT 2b. For more details, see Appendix G.

As this star has not previously been characterized in detail, we modeled its spectral energy distribution (SED) to constrain its physical properties. We performed a χ^2 fit of 17 photometric points from TYCHO (E. Høg et al. 2000), Pan-STARRS (K. C. Chambers et al. 2016), Gaia DR3 (Gaia Collaboration et al. 2023), DENIS (N. Epchtein et al. 1999), and the Two Mass All Sky Survey (2MASS; R. M. Cutri et al. 2003) to synthetic models from BT-Settl CIFIST (F. Allard et al. 2013) using the Virtual Observatory SED Analyzer (VOSA; A. Bayo et al. 2008). Photometric data from the Wide-field Infrared Survey Explorer (WISE; R. M. Cutri et al. 2012) were not included in the fit because VOSA identified photometric excess starting at band W1 (3.4 μm). The extinction was constrained to the 1σ-range derived in Appendix A.1, $A_V = 0.136 \pm 0.087$ mag. While this does not account for possible extinction from the disk itself, we expect such effects to be minimal due to the disk's ~45° inclination (see Section 4) and a cleared inner gap, making the interstellar extinction a reasonable approximation. The other model

Table 1
Stellar Parameters of WISPIT 2

Parameter	Value	References
Gaia DR3	4207586980945067648	(1)
2MASS	J19231702-0740550	(2)
WISE	J192317.04-074055.2	(3)
TIC	98898373	(4)
TYC	5709-354-1	(5)
R.A.* α [deg]	290.82100005622	(1)
Decl.* δ [deg]	−07.68208608363	(1)
Parallax ϖ [mas]	7.4649 ± 0.0214	(1)
Distance d [pc]	$133.35^{+0.37}_{-0.38}$	(6)
pmra μ_α [mas yr^{-1}]	6.308 ± 0.024	(1)
pmdec μ_δ [mas yr^{-1}]	−27.138 ± 0.018	(1)
v_r [km/s]	−16.23 ± 14.58	(1)
G [mag]	11.186381 ± 0.003952	(1)
$B_p - R_p$	1.377451	(1)
$B_p - G$	0.550725	(1)
$G - R_p$	0.826726	(1)
J [mag]	9.310 ± 0.044	(2)
H [mag]	8.591 ± 0.078	(2)
K_s [mag]	8.577 ± 0.021	(2)
W1 [mag]	8.475 ± 0.028	(3)
W2 [mag]	8.444 ± 0.027	(3)
W3 [mag]	8.046 ± 0.027	(3)
W4 [mag]	3.300 ± 0.027	(3)
FUV	20.373 ± 0.217	(7)
NUV	18.168 ± 0.052	(7)
P_{rot} [day]	4.7004	(8)
A_V [mag]	0.171 ± 0.050	(9)
T_{eff} [K]	4400 ± 50	(9)
$\log g$ [dex]	4.00 ± 0.25	(9)
L_{bol} [$L_\odot$]	0.699 ± 0.021	(9)
R [$R_\odot$]	1.418 ± 0.004	(9)
Age [Myr]	$5.1^{+2.4}_{-1.3}$	(9)
Mass [$M_\odot$]	$1.08^{+0.06}_{-0.17}$	(9)

Note. *=ICRS, epoch J2016.0.

References: (1) Gaia Collaboration et al. (2023), (2) R. M. Cutri et al. (2003), (3) R. M. Cutri et al. (2012), (4) K. G. Stassun et al. (2019), (5) E. Høg et al. (2000), (6) C. A. L. Bailer-Jones et al. (2021), (7) L. Bianchi et al. (2011), (8) C. L. Watson et al. (2006), (9) This work.

parameters for the fit were constrained to be in ranges $3000 \leqslant T_{\mathrm{eff}} \leqslant 6000$, and $3.5 \leqslant \log g \leqslant 4.5$. We adopted the best-fit model consistent with L. Prato & M. Simon (2023), and used the resulting bolometric luminosity of $L_{\mathrm{bol}} = 0.699 \pm 0.021\, L_\odot$ and temperature of $T_{\mathrm{eff}} = 4400 \pm 50$ K to retrieve a mass of $1.08^{+0.06}_{-0.17}\, M_\odot$ and age of $5.1^{+2.4}_{-1.3}$ Myr by comparing to BHAC15 (I. Baraffe et al. 2015) isochrones. The uncertainties are adjusted to account for systemic errors due to choice of stellar evolution model (see Appendix A.3). While on the lower end, the resulting age is consistent with that of the group to which WISPIT 2 likely belongs. From this, we conclude that WISPIT 2 is a young (∼5 Myr) solar-mass star.

The parameters obtained from the SED fit, as well as the mass and age derived from the isochrone fit, are provided in Table 1. Figure 2 presents the best-fit synthetic spectrum overlaid on the photometry, which was dereddened by VOSA using the extinction law by E. L. Fitzpatrick (1999) improved by R. Indebetouw et al. (2005) in the infrared. This SED already reveals an increased infrared excess at W4 (22 μm), hinting at the presence of a disk.

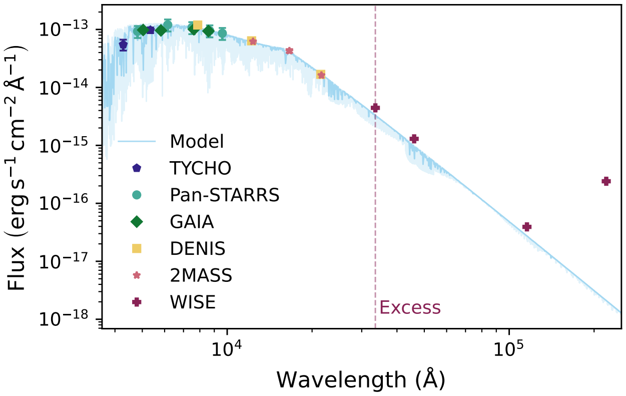

Figure 2. The SED of WISPIT 2 is presented here. Photometric data from various sources are shown with colored markers. The blue curve represents the best-fit BT-Settle-CIFIST model ($\chi^2 = 7.94$), with the low-resolution (high-opacity) version overlaid on the high-resolution (low-opacity) model.

3. Observations and Data Processing

3.1. Description of Observations

All observations were performed at VLT with the Spectro-Polarimetric High-contrast Exoplanet REsearch (SPHERE) instrument (J. L. Beuzit et al. 2019) using the Infrared Dual-band Imager and Spectrograph (IRDIS; K. Dohlen et al. 2008) camera. We present four different observational epochs taken on 2023 October 19, 2024 October 4, 2025 October 21, and 2025 April 26. Details on the exposure settings and weather conditions for all epochs are given in Table 2. In the following, we give a brief summary.

The first two observational epochs were taken as part of the main WISPIT survey program (R. F. van Capelleveen et al. 2025, in preparation). Both of these observation epochs were taken in the H band in the classical imaging mode with pupil stabilization. These two epochs have a total exposure time of 4.3 minutes each. The observation epoch on 2025 March 21 was taken in the broadband H-filter with IRDIS Dual Polarization Imaging (DPI) mode (J. de Boer et al. 2020; R. G. van Holstein et al. 2020). A total of 12 polarimetric cycles were recorded, each consisting of the usual four images taken at different half wave plate positions. This led to a total exposure time of 51.2 minutes. While the observation sequence was taken in pupil stabilized mode to maximize polarimetric efficiency, the overall parallactic field rotation was small ($2\overset{\circ}{.}3$). The data set taken on 2025 April 26 was taken in an identical manner using the broadband K_s-filter and additionally using the "star-hopping" technique (Z. Wahhaj et al. 2021). This technique alternates every ∼10 minutes between science target and reference star. Similar to the previous observation that we obtained 12 polarimetric cycles on the science target for a total exposure time of 51.2 minutes. For the reference star, we recorded 20 frames interspersed with the science target and with the same individual frame exposure time. The observation sequence was carried out in pupil stabilized mode to allow for multiple differential imaging processing approaches as well as to maximize polarimetric efficiency. A total parallactic angle rotation of $27\overset{\circ}{.}5$ was recorded.

Table 2
SPHERE/IRDIS Observations of WISPIT 2

Observation Date (yyyy-mm-dd)	Filter	Coronagraph	NEXP × NDIT × DIT (1 × 1 × s)	ω (arcsec)	X	τ_0 (ms)
2023-10-19	H	N_ALC_YJH_S	4×2×32	0.545 ± 0.005	1.284 ± 0.005	4.1 ± 0.3
2024-10-04	H	N_ALC_YJH_S	4×2×32	0.990 ± 0.097	1.397 ± 0.007	4.5 ± 0.3
2025-03-21	H	N_ALC_YJH_S	48×1×64	0.390 ± 0.048	1.451 ± 0.063	5.7 ± 1.3
2025-04-26	K_s	N_ALC_Ks	48×1×64	0.275 ± 0.037	1.146 ± 0.067	7.4 ± 1.5

Note. Observation setup and conditions for all WISPIT 2 observations. All filters are SPHERE broadband filters. The total integration time is the product of the number of exposures (NEXP), the number of subintegrations per exposure (NDIT), and the detector integration time (DIT). The seeing is denoted by ω, the airmass by X, and the coherence time by τ_0.

3.2. Data Reduction

We used all four SPHERE observation epochs to produce total intensity images of the WISPIT 2 system. Total intensity observations are sensitive to scattered light from the circumstellar dust, as well as the thermal emission of embedded planets. Depending on the observation epoch, we used several differential imaging post-processing techniques to remove the stellar speckle field from the images. We summarize these for all observation epochs along with the standard data reduction.

All SPHERE total intensity observations in broadband filters were (pre-)processed with `PynPoint` (A. Amara & S. P. Quanz 2012; T. Stolker et al. 2019). The reduction workflow includes bad-pixel correction, flat-fielding, sky subtraction, and anamorphic distortion correction. The anamorphic distortion was corrected by scaling the y-axis by a factor of 1.0062 ± 0.0002, following the procedure outlined in the SPHERE documentation[10] and described by A.-L. Maire et al. (2016). Images were aligned to the sky's parallactic angle and corrected for the pupil offset of 135.99 ± 0.11 deg, and an additional rotation of 1.76 ± 0.04 deg was applied to correct for the true North offset (A.-L. Maire et al. 2021). The pixel scales for astrometric calibration are 12.246 ± 0.009 mas yr^{-1} in the H band and 12.266 ± 0.009 mas yr^{-1} in the K_s band based on the 5 yr analysis of SPHERE astrometric calibration data presented in A.-L. Maire et al. (2021).

Due to the short integration time, the two initial H-band observations taken in 2023 and 2024 only have $\sim 1^\circ$ of field rotation, which makes them unsuitable for reduction with angular differential imaging (ADI). Instead, we used reference star differential imaging (RDI; B. A. Smith & R. J. Terrile 1984; D. Lafrenière et al. 2009; A. M. Lagrange et al. 2009) with principal component analysis (PCA; A. Amara & S. P. Quanz 2012; R. Soummer et al. 2012). We leveraged observations from YSES to create a reference library. We built on the reference library used in A. J. Bohn et al. (2021) and excluded YSES observations affected by image misalignment, binarity, the presence of contaminating sources in the field of view, or poor image quality, resulting in a library of 61 observations comprising 340 frames. The observations in this library are listed in Table 10 in Appendix H. From this set, for each WISPIT 2 observation, the 275 frames with the highest correlation based on mean squared error (MSE) were selected for the reference library, a strategy proven to be effective in increasing RDI performance (e.g., G. Ruane et al. 2019; C. Xie et al. 2022; A. Sanghi et al. 2024). We produced two different sets of reductions for each of these two epochs. Initially, we performed RDI with 50 principal components on the entire image. The results are shown in the first two panels of Figure 3 revealing extended circumstellar disk structure. To increase sensitivity and minimize over-subtraction in the potential planet-hosting gap between the surrounding bright rings, we isolated the gap with an elliptical mask and applied the reduction routine separately to the gap and the rest of the image. The results of this approach, using 30 principal components for the 2023 epoch and 40 for the 2024 epoch, are displayed in Figure 4.

As there was very little parallactic field rotation in the following H-band epoch taken in 2025, and no reference library was available for the SPHERE polarimetric imaging mode, we did not perform a total intensity differential imaging reduction for this data set.

The 2025 K_s-band observation sequence had significant parallactic angle rotation and, thus, allowed for ADI to be performed; additionally, the recorded interspersed reference star images allowed also for dedicated RDI. Initially we performed classical ADI (cADI) as outlined by C. Marois et al. (2006). The result is shown in Figure 3. We then performed more aggressive processing using PCA-based ADI (PCA-ADI) with `PynPoint`, as outlined in A. Amara & S. P. Quanz (2012), focusing on the embedded planet. We used five principal components for this reduction, the result of which is shown in Figure 4. Finally, we performed PCA-based RDI on the data set using the dedicated reference star observations. To prevent over-subtraction due to the bright circumstellar disk structures, we followed the approach outlined in C. Ginski et al. (2021) for iterative reference star differential imaging (iRDI).[11] The result of this approach is shown in Figures 3 and 4.

Both the H- and K_s-band 2025 observations were performed in the IRDIS DPI mode, making them suitable for polarimetric differential imaging (PDI; J. R. Kuhn et al. 2001). While PDI is one of the best techniques to reveal (polarized) scattered light from circumstellar material (see, e.g., the discussion in M. Benisty et al. 2023), it is not sensitive to unpolarized thermal emission of embedded planets. PDI was performed using the IRDIS Data reduction for Accurate Polarimetry (IRDAP; R. G. van Holstein et al. 2020) pipeline. As a result, IRDAP produces the Stokes Q and U images that contain the linearly polarized signal from the circumstellar disk, while having removed the unpolarized signal from the central star. Using an instrument model as

---

[10] SPHERE manuals: https://www.eso.org/sci/facilities/paranal/instruments/sphere/doc.html.

[11] We note that this approach is not suitable for the initial shorter H-band observation epochs as it requires a dedicated reference star sequence and does not work well with a library of observations.

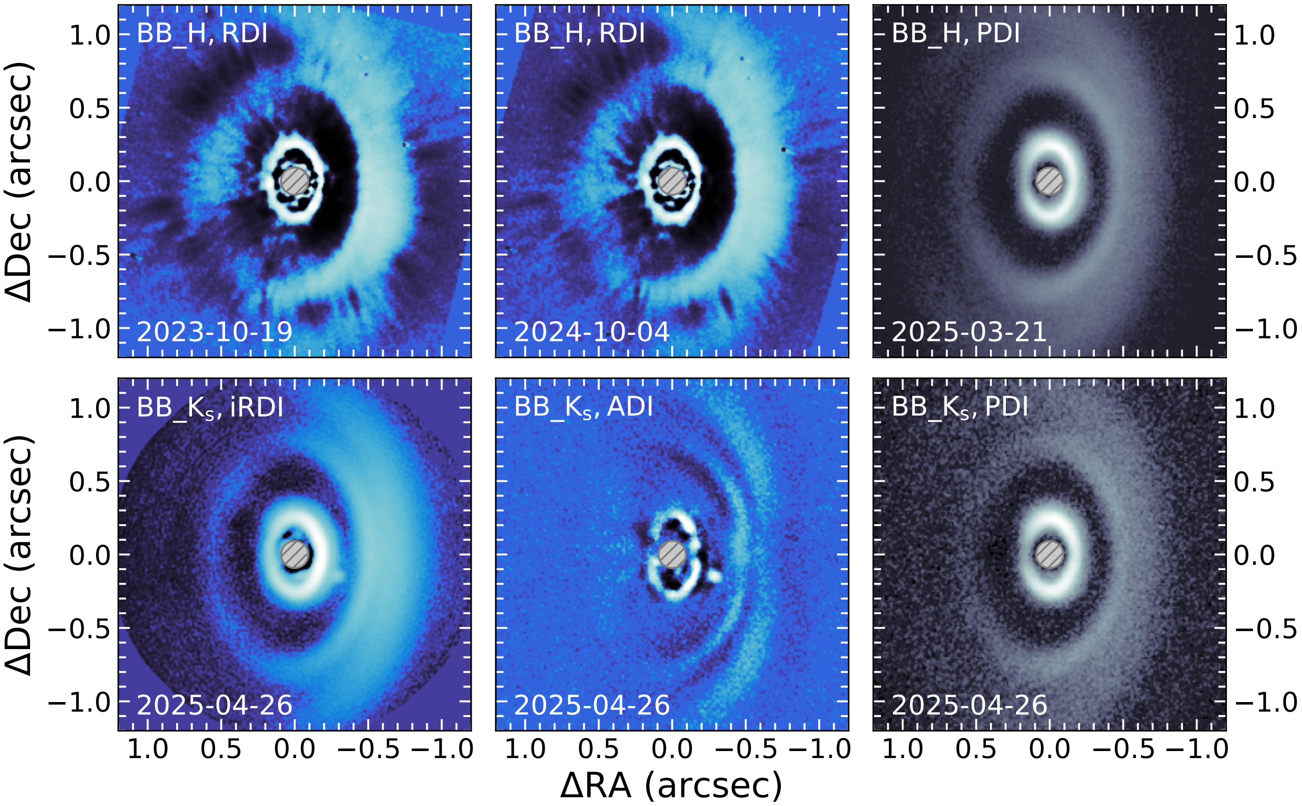

Figure 3. SPHERE/IRDIS observations of the WISPIT 2 system are shown here. The gray, hashed disk in the image center indicates the size of the coronagraphic mask. The differential imaging method and observed wave band for each image are indicated in the top-left corner. Blue-hued images reduced with the ADI or RDI (50 principal components) methods are showing total intensity, sensitive to disk scattered light and thermal emission from embedded planets. The gray-hued images are Q_ϕ images (reduced with the PDI method) showing linearly polarized scattered light, not sensitive to thermal emission.

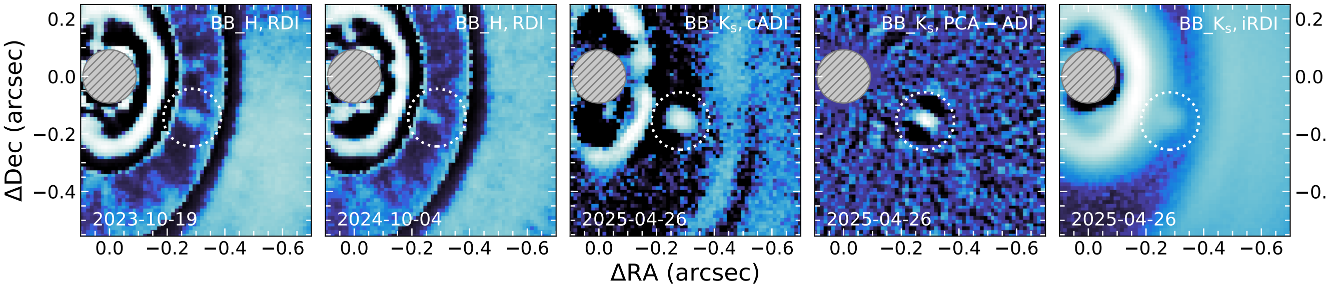

Figure 4. All detections of the embedded planet WISPIT 2b in the various observation epochs and filters are shown. We indicate the embedded planet position with a white, dotted circle. The coronagraph position is indicated with a gray, hashed mask. For the 2025 K_s-band data, we show that the embedded planet is recovered with classical and PCA-based ADI as well as in iRDI.

well as dedicated measurements within the final Q and U images, IRDAP also removes residual stellar polarization, which can be induced either by the telescope and instrument or by interstellar or local dust around the star. For the polarimetric observations, we generally show the Q_ϕ images, which contain the expected azimuthally polarized scattered light signal from single scattering events as positive signal (see, e.g., J. D. Monnier et al. 2019, for a description of the Q_ϕ formalism). The polarized light H- and K_s-band images are both shown in Figure 3. Additionally, we show the associated Stokes Q and U images in H band and K_s band in Figures 15 and 16 in Appendix B, respectively.

4. An Extended Multi-ringed Disk Seen in Scattered Light

Our SPHERE observations resolve for the first time an extended circumstellar disk surrounding WISPIT 2. Using the polarimetric H-band image as a reference, we find detectable signal out to $2\overset{''}{.}8$ (380 au) from the star along the north–south direction, which appears to coincide with the major axis of the disk (forward scattering, near side to the west). Within this region, the disk appears highly structured with a set of four concentric rings separated by gaps of different sizes and contrast. We indicate the individual rings and gaps in Figure 5. We used an outside-in labeling strategy for the various structures, as future observations at higher angular resolutions may well detect additional structures farther in. We detect no clear scattered light signal inside ring 3 and down to the coronagraphic mask, which may indicate that there is indeed a cavity in the disk at this position (also seen at z' band in L. M. Close et al. 2025b, companion Letter 2). By far the most prominent gap in the disk is located between ring 2 and ring 3.

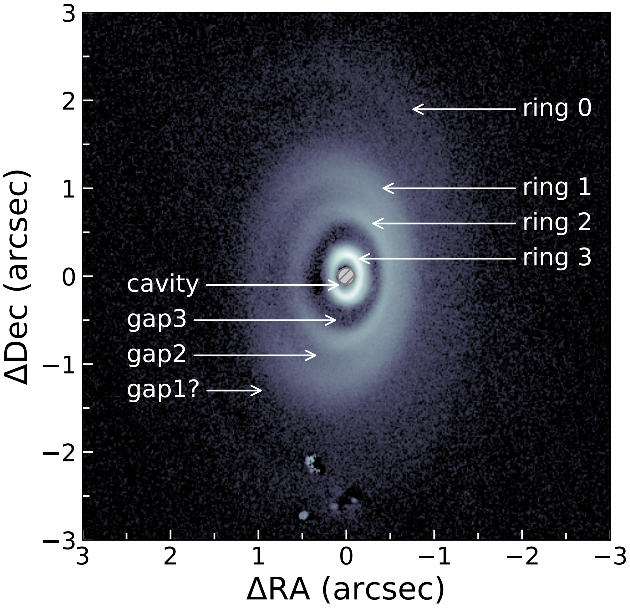

Figure 5. Polarized light Q_ϕ image of the WISPIT 2 system taken in the H band. We indicate the various substructures that we are detecting within the scattered light signal of the planet-forming disk. Clusters of bad pixels from the detector are seen near the lower edge of the image.

To obtain an overall picture of the disk morphology, we fitted simple geometrical models to the individual rings. Features were extracted using a semiautomatic algorithm that involves edge detection and subsequent ellipse fitting based on the points extracted. For the edge detection, we used radial cuts from the stellar position to the outer disk regions. For the well-defined rings 1 and 2, we found the ring position by fitting 1D Gaussian profiles to the radial cuts. For the innermost ring (ring 3), this method proved problematic due to its somewhat extended flux toward the West, which may be related to the bottom side of the visible disk, as we discuss in Appendix C. In this case, we used the simple maximum of the disk flux along each radial profile instead. For the outermost ring (ring 0), the signal was too faint for Gaussian fitting; thus, in this case, we also used the largest value in the profile (including some thresholding to exclude spurious data points).

In addition to the visible rings, we also measured the position and width of the gap between rings 2 and 3 by applying inverse Gaussian fitting, where the algorithm targets the intensity minima along the pixel line rather than the peaks. The results of each of the positional fits are listed in Appendix E. The approximate radial locations for ring 0–3 are at 316, 164, 97, and 38 au. The center of the gap is located at approximately 69 au, and the gap has a width of 59 au in the H-band image, based on the FWHM of the inverse Gaussian used for fitting. We find an average inclination of $43\overset{\circ}{.}99 \pm 0\overset{\circ}{.}87$ and position angle of $358\overset{\circ}{.}7 \pm 1\overset{\circ}{.}1$ in the H band, and $45\overset{\circ}{.}86 \pm 1\overset{\circ}{.}27$ and $359\overset{\circ}{.}3 \pm 2\overset{\circ}{.}3$ in the K_s band, respectively (see Figure 18 in Appendix E for convention).

Following J. de Boer et al. (2016), we used the offset of the ellipse center from the stellar position along the minor axis to measure the height of the disk scattering surface above the disk midplane. This assumes that the identified rings are not significantly eccentric, as an inherent eccentricity can also lead to a center offset along the minor disk axis independent of the disk vertical structure. Figure 6 shows the aspect ratio (the disk height divided by the radial separation) h/r versus r, which can be described by a power law

$$\frac{h}{r} = \frac{h_0}{r_0}\left(\frac{r}{r_0}\right)^{\alpha-1}, \tag{1}$$

where h_0 describes the height at radius r_0, and α is the flaring index. We fit this power law to the data using ring 1 as the reference point ($h_0 = 24.0$ au, $r_0 = 163.6$ au), yielding flaring indices of 1.77 in the H band and 2.22 in the K_s band. Previous determinations of the flaring index include 1.22 from H. Avenhaus et al. (2018) for a joint fit of a set of five T Tauri stars and 1.73 from C. Ginski et al. (2016) for the extreme case of the Herbig star HD 97048. Our H-band result closely matches the latter, while the K_s-band flaring index is significantly higher. This high value is driven by the strong discrepancy between the relatively flat inner disk (ring 3) and the strongly flared outer disk (rings 1 and 2). As is visible in Figure 6 (right panel), the inner disk (ring 3) in the WISPIT 2 system is indeed among the gas-rich disks with the lowest aspect ratio reported in the literature to date (C. Ginski et al. 2016, 2024; H. Avenhaus et al. 2018). While the disk vertical profile is then subsequently rising steeply (as indicated by the large flaring index we find), the disk vertical extent remains on the low end compared to the full literature population with the outermost well-defined ring 1 having only an aspect ratio of 0.15 ± 0.01. We also note that the overall aspect ratio that we recover is smaller at all radial locations for the K_s band than for the H band. This is an expected behavior related to lower dust opacities at longer wavelengths, which look deeper into the disk at longer wavelengths.

5. Thermal Emission from an Embedded Planet

5.1. Astrometric Analysis

We extracted the astrometry and photometry of the observation in the K_s band following the methods of T. Stolker et al. (2020b). We used the `SimplexMinimizationModule` of `PynPoint` to first obtain an approximate position and flux of the companion by minimizing the flux residuals, evaluated in a 5 pixel aperture around the injection position, with a downhill simplex method. We then performed Bayesian inference using Markov Chain Monte Carlo (MCMC; D. J. C. MacKay 2003) to sample from the posterior distribution, using the `MCMCsamplingModule`. The systemic uncertainties of the injection and minimization approach are derived with `SystematicErrorModule`, which injects positive artificial companions with the same magnitude contrast and at the same radial separation as WISPIT 2b at positions equidistantly distributed in polar space, and then extracts the astrometry and photometry of these artificial companions with the same method as described above. The error on the pixel position of the companion is the combination of the standard deviation across the injected positions and the astrometric uncertainty of the fit of the companion.

The planet signal is significantly less prominent in the H-band observations than in the K_s-band observations due to shorter exposures and negligible field rotation. As a result, extracting the astrometry from the H-band snapshots requires a different approach. In these observations, the region near the companion is dominated by speckle noise, partially introduced

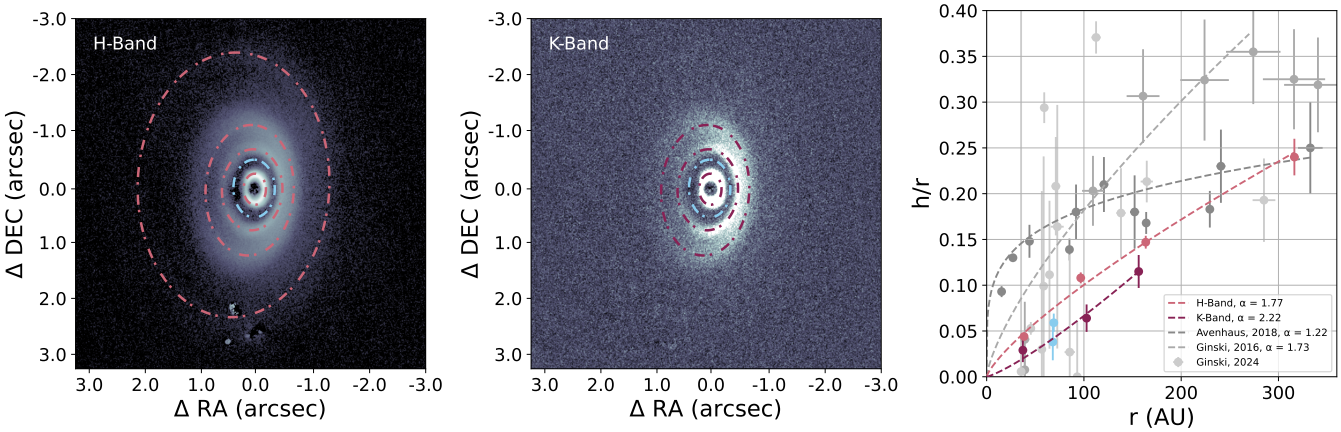

Figure 6. Left and middle panels: geometric fitting of the disk in both *H*-band and K_s-band images. Right panel: the aspect ratio (h/r) vs. radius (au) of both bands. For comparison, we include the literature measurements of C. Ginski et al. (2016), H. Avenhaus et al. (2018),and C. Ginski et al. (2024) for a total of 17 disks (some of which also have a multiple ringed substructure) as gray data points.

Table 3
Astrometric and Photometric Measurements of WISPIT 2b

Observation Date (yyyy-mm-dd)	Filter	Separation (mas)	Position Angle (deg)	Magnitude Contrast (mag)	Absolute Magnitude (mag)
2023-10-19	H	318.9 ± 2.2	244.5 ± 0.2	$9.8^{+0.4}_{-0.3}$	$12.8^{+0.4}_{-0.3}$
2024-10-04	H	313.7 ± 3.5	242.7 ± 0.4	$10.6^{+0.6}_{-0.4}$	$13.5^{+0.6}_{-0.4}$
2025-04-26	K_s	320.1 ± 2.1	242.1 ± 0.2	$9.0^{+0.04}_{-0.04}$	$11.95^{+0.09}_{-0.09}$

by the RDI/PCA subtraction. To robustly extract the position of the companion, we performed a 2D Gaussian fit to each of the eight individual frames, using the residuals from all RDI/PCA reductions resulting from subtraction of 0 to 100 principal components in steps of 2, with bounds applied to the fit parameters. For each of the eight frames, this yielded 50 pixel position measurements, with uncertainties from the covariance matrix of the Gaussian fit. Details of the fitting routine and bounds are provided in Appendix D. For each frame, we filtered out unsuccessful fits—specifically, fits that failed to converge, reached imposed bounds, or had positional uncertainties exceeding 100 pixels (more than half the size of the cropped frame). The remaining fits were averaged per frame, with uncertainties derived from both the spread in measurements and the uncertainties of the individual fits. The final astrometric measurement was obtained by computing the weighted mean and standard deviation across the eight independent frames.

In conversion from pixel positions to separation (arcseconds) and position angle (degrees) of both *H*-band and K_s-band observations, uncertainties in pixel scale, true North correction, and pupil offset (as outlined in Section 3.2), as well as the centering precision of 2.5 mas of the star behind the coronagraph, were included in the error budget. The resulting astrometric measurements are reported in Table 3.

The predicted parallactic motion of a stationary background object was calculated using the Gaia DR3 distance to WISPIT 2 (see Table 1). Figure 7 plots the measured companion positions for all three epochs relative to these background tracks, confirming that the companion is inconsistent with a background source.

Given our astrometric measurements of the planet, we tested whether the change in position relative to the central star (apparent in Figure 7), is consistent with the expected orbital motion of a low-mass planet. However, the astrometric uncertainties for the *H*-band epoch on 2024 October 4 are notably larger than those of the other two epochs, as also seen in Figure 7, primarily due to poorer observing conditions (see the higher seeing values in Table 2). We also note increased contamination by residuals from the bright inner ring—compounded by the fainter planet signal—which biases the Gaussian fit center toward ring 3. Given these limitations, we

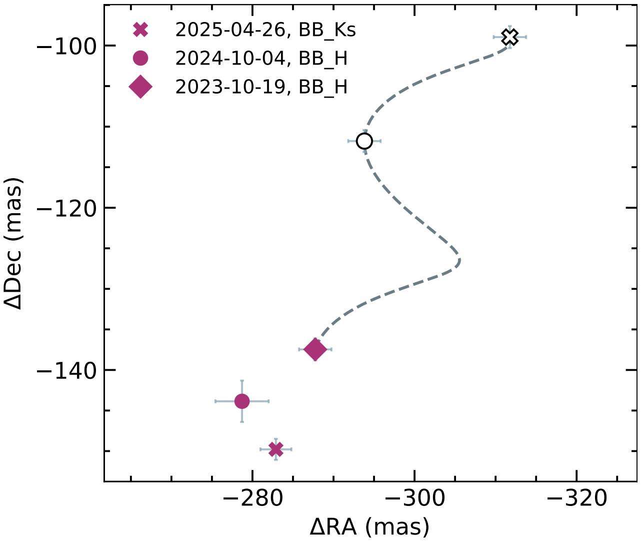

Figure 7. Proper-motion analysis of WISPIT 2b. Each epoch is represented by a unique marker shape: diamond (2023), circle (2024), and cross (2025). The colored version of each marker denotes the measured position of the companion. The unfilled (black outline, white center) version of each marker shows the expected position of the source if it were a stationary background object. The dashed curve illustrates the parallactic motion of such a background object from first to last epoch.

excluded the 2024 epoch from the orbital fit and used only the first (H band, 2023 October 19) and last (K_s band 2025, April 26) epochs, which gives us the longest time baseline currently available for the system.

The orbital fit was performed using the `orbitize!` package (S. Blunt et al. 2020), using the Orbits For The Impatient (OFTI) algorithm (S. Blunt et al. 2017) as it is particularly well suited for systems where only a small fraction of the orbital motion has been observed, as is the case with WISPIT 2b. As the planet is located in the disk gap, and the disk appears very symmetric and unperturbed in scattered light, we assume that the planet does not cross the disk. For this initial orbital analysis, we further assume that the planet's orbit is coplanar and aligned with the disk. These assumptions result in a fixed value for the orbital inclination of 135° (encoding also the clockwise orbital motion of the planet). The angle of the ascending node was fixed at 0°. These values are consistent with our disk geometric fit presented in Section 4. For the semimajor axis, we used the default log-uniform prior with lower and upper bounds initially set to 40 au and 100 au, respectively. The upper bound was purposefully chosen to be slightly larger than the outer edge of the disk gap to prevent a pile-up of solutions in the posterior distribution at the parameter boundary. After the fits were concluded, we then down-selected only solutions with a maximum semimajor axis of 70 au, which are then fully contained within the disk gap. Finally, we chose the default Gaussian prior for the total system mass centered at $1\,M_\odot$ and with a standard deviation of $0.1\,M_\odot$. A selection of orbital bundles from the fitting routine is shown in Figure 8. According to the histogram in the bottom panel of Figure 8, the most probable semimajor axis is ∼ 57 au, which falls in the inner region of the gap between ring 3 and the deepest part of gap 3. Despite this clear peak, the distribution shows that this semimajor axis may extend upward of 60 au, which could place the planet at the deepest part of gap 3, where it may be the sole contributor to the dust depletion. With current constraints, the distribution of eccentricities derived from the orbital fit is heavily skewed toward low values, with 93% having $e < 0.3$ and 77% having $e < 0.2$.

5.2. Photometric Analysis

The K_s-band flux was retrieved following the methods of T. Stolker et al. (2020b), as described in Section 5.1.

To measure the planet flux in our short WISPIT H-band observations of 2023 and 2024, we used the RDI reductions presented in Figure 4. For the 2023 epoch, we used the median-combined residuals from RDI/PCA processing with 30 principal components. Due to highly variable observing conditions during the 2024 epoch, we selected a subset of frames based on point-source visibility and low rms noise. The final 2024 reduction uses median-combined residuals from frames 2, 4, 5, and 8 (of eight total), processed with RDI/PCA using 40 principal components. As a calibrator, we used the flux images taken of the central star in the same observation sequences, where the star was moved away from the coronagraph, and a neutral density filter was inserted to prevent saturation. The planet flux was measured inside an aperture with a radius of 4 pixels. To account for RDI over-subtraction, we estimated the local background with the same aperture along the disk gap near the planet. For the 2023 observation, we find an H-band contrast between planet and central star of $9.8^{+0.4}_{-0.3}$ mag. For the 2024 observation, we measure $10.6^{+0.6}_{-0.4}$ mag. While this is consistent within uncertainties with the magnitude contrast derived from the 2023 epoch, it is notably higher.

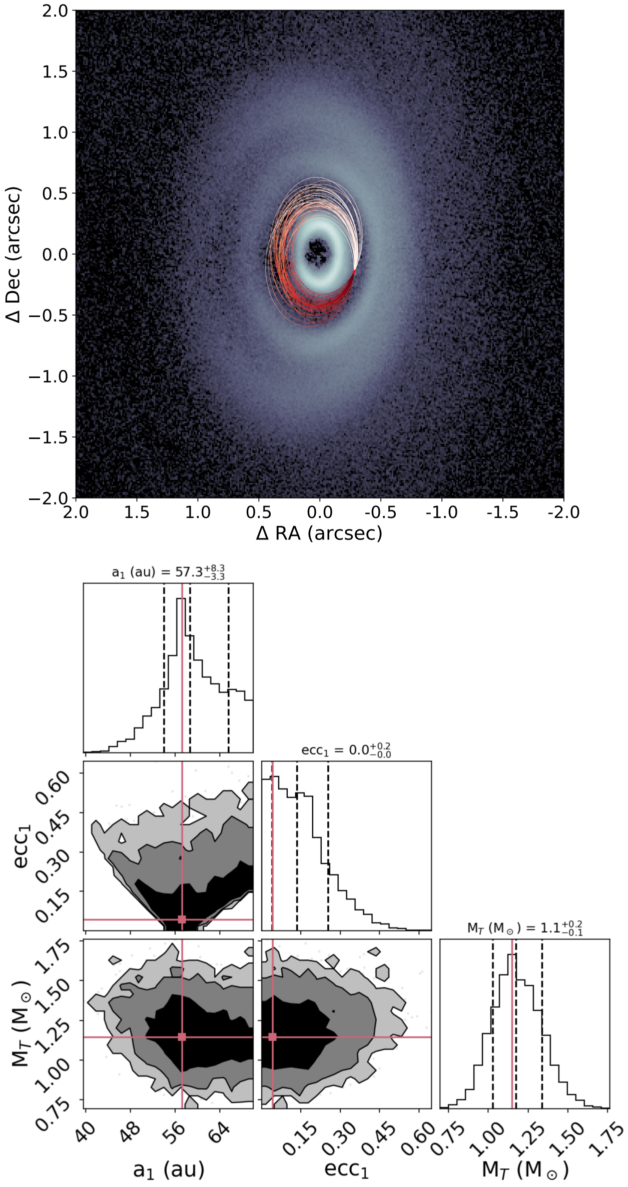

Figure 8. Top panel: predicted orbits of the planet (known astrometry denoted by red star) overlaid on the H-band polarized scattered light image. Bottom panel: extracted orbital elements and total system mass.

In both epochs, a primary source of uncertainty is the background variation within the disk gap after the RDI reduction. However, in 2024, the main contributors to the uncertainty are the highly variable and overall poorer observing conditions (see Table 2), which led to nondetections in some frames and only marginal detections in others. As a result, the embedded planet signal appears significantly fainter and is more likely to be partially removed in RDI processing, as also discussed in Section 3 and visually evident in the residuals shown in Figure 4. Given these challenges associated with the 2024 data and its larger uncertainties, we adopt the magnitude derived from the 2023 epoch for further analysis.

The color–magnitude diagram of the companion is shown in Figure 9, along with 5.11 Myr AMES-COND and AMES-

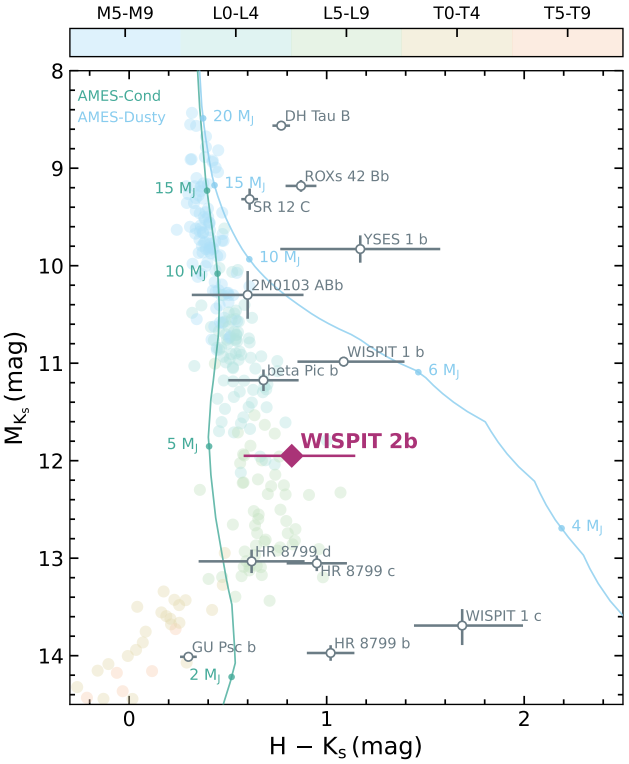

Figure 9. Color–magnitude diagram of WISPIT 2b, with field brown dwarfs of various spectral types and confirmed planetary companions. Teal and cyan tracks show 5.1 Myr AMES-COND and AMES-DUSTY isochrones, respectively. WISPIT 2b is marked in purple.

DUSTY isochrones (G. Chabrier et al. 2000; F. Allard et al. 2001) and other known planets with available H and K_s magnitudes. To estimate the mass of the companion, we sampled from its asymmetric H-magnitude, K_s-magnitude, and age distributions. Here, the age is the previously derived stellar age of $5.1^{+2.4}_{-1.3}$ Myr (see Section 2). We used `species` (T. Stolker et al. 2020b) to retrieve color–magnitude data from the AMES isochrones, and estimated the companion's mass by interpolating the sampled K_s-band magnitude onto the AMES-COND and AMES-DUSTY evolutionary model grids separately. While we note that both models give a consistent mass range for WISPIT 2b, we obtained a final mass estimate by interpolating the $H - K_s$ color between the two isochrones. The derived masses from both models as well as the interpolated mass are presented in Table 4; the final adopted mass is $4.9^{+0.9}_{-0.6}$ $M_{\rm Jup}$. Both the photometric measurements and the resulting mass are consistent with a planetary classification of the companion.

We caution that the reported uncertainty may be underestimated due to various factors that require additional data and further analysis, such as the age of the star; spectral analysis is necessary to more accurately characterize WISPIT 2 , which may, in turn, affect the mass estimate. Additionally, there are factors that cannot be quantified with the current data. The most significant of these is the unknown extinction that could potentially be introduced by a CPD or by the circumstellar disk itself, as was inferred in the case of PDS 70b (V. Christiaens et al. 2019). However, a comparison with PDS 70b suggests a lower degree of extinction in our case. Using the H-band magnitude of 14.9 ± 0.90 from D. Mesa et al. (2019) and K_s-band magnitude of 11.37 ± 0.30 from Z. Wahhaj et al. (2024), PDS 70b has a significantly redder $H - K_s$ color of 3.53 ± 0.95, placing it far to the right of the AMES-DUSTY track in Figure 9, and even outside the plotted bounds. In contrast, the color of WISPIT 2b lies between the AMES-COND and AMES-DUSTY isochrones, indicating significantly less reddening and pointing to a less substantial and/or more dust-depleted CPD. This is compounded by the lack of a CPD signal in polarized light from our K_s-band data, especially given the high signal-to-noise ratio. Both the color and lack of polarized emission suggest that the extinction is likely to be less severe than in the PDS 70b case. While we cannot reliably constrain this extinction, WISPIT 2b's low mass, which is well below the deuterium burning limit, makes it highly unlikely that additional extinction would alter the conclusion regarding its planetary nature. Further observations and analysis are required to improve upon the companion's mass accuracy.

Table 4
Mass of WISPIT 2b from Evolutionary Models

Model	Mass ($M_{\rm Jup}$)
AMES-COND	$4.87^{+0.98}_{-0.59}$
AMES-DUSTY	$4.78^{+0.94}_{-0.54}$
Interpolated	$\mathbf{4.85^{+0.94}_{-0.58}}$

Note. Mass estimates for WISPIT 2b using AMES-COND and AMES-DUSTY evolutionary tracks. The final value in the *Interpolated* row is derived by interpolating the $H - K_s$ color between both model grids.

6. Planet–Disk Interaction

The opening of gaps in the planet-forming disk by embedded planets is predicted by theoretical models of planet–disk interaction and arises from the gravitational torques that the planet exerts on the surrounding disk gas and the resulting angular momentum exchange (see, e.g., S.-J. Paardekooper & G. Mellema 2006; J. Bae et al. 2017). The relation between the mass of the planet and the width of the gap that is opened by it has been the subject of detailed hydrodynamic studies. To comparatively assess the estimated planet mass derived via photometric analysis, we implemented the K. D. Kanagawa et al. (2016) and S. Zhang et al. (2018) models to investigate the relationship between gap width and the star–planet mass ratio for the case of the WISPIT 2 system. The K. D. Kanagawa et al. (2016) model focuses exclusively on the gas surface density, creating a more idealized framework. In contrast, the S. Zhang et al. (2018) model incorporates both gas and dust as coupled but distinct fluids, simulating their interaction to directly model the dust emission gaps observed by ALMA. Additionally, the two models adopt different definitions for the gap width parameter, $\Delta_{\rm gap}$. K. D. Kanagawa et al. (2016) defined it as the absolute radial width $r_{\rm out} - r_{\rm in}$, while S. Zhang et al. (2018) normalized it to the gap location using $\frac{r_{\rm out} - r_{\rm in}}{r_{\rm out}}$.

Figure 10 illustrates the increasing trend of the mass ratio q, with gap width for various disk viscosity parameters α (N. I. Shakura & R. A. Sunyaev 1976). Using the gap width estimated from the Gaussian fitting of the dust rings (see Table 8 in Appendix E), ~59 au measured along the disk

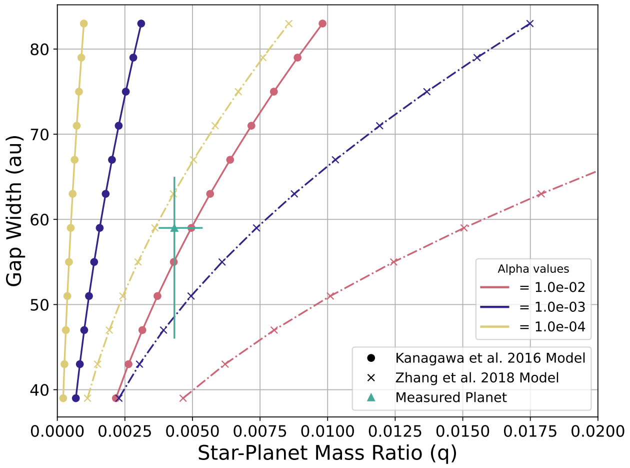

Figure 10. Relationship between the gap width and the mass ratio q. Here, the K. D. Kanagawa et al. (2016) model is represented by the dots, and the S. Zhang et al. (2018) is represented by the crosses. A triangle marker has been inserted to show the star–planet mass ratio based on magnitude and age estimates.

major axis in the H band, we apply the respective models:

$$\frac{M_p}{M_*} = 2.1 \times 10^{-3}\left(\frac{\Delta_{\text{gap}}}{R_p}\right)^2 \times \left(\frac{h_p}{0.05R_p}\right)^{\frac{3}{2}}\left(\frac{\alpha}{10^{-3}}\right)^{\frac{1}{2}}, \tag{2}$$

and

$$\frac{K'}{0.014} = \frac{q}{0.001}\left(\frac{\frac{h}{r}}{0.07}\right)^{-0.18}\left(\frac{\alpha}{10^{-3}}\right)^{-0.31}, \tag{3}$$

where the fitting parameter K' is $K' = A\Delta^B$, and the best-fit gas surface density parameters of A and B are taken from Table 1 of S. Zhang et al. (2018).

Considering the full range of viscosity α parameters from 10^{-4} to 10^{-2}, we get mass ranges for the gap-opening planet of 0.5 M_{Jup}–5.3 M_{Jup} for the K. D. Kanagawa et al. (2016) models and 4 M_{Jup}–16 M_{Jup} for the S. Zhang et al. (2018) models. Our photometrically estimated planet mass of $4.9^{+0.9}_{-0.6}$ M_{Jup} lies thus slightly above the upper end of the former and within the lower end of the latter models. Thus, in principle, the scattered light gap is consistent with being opened by the detected planet, dependent on the disk viscosity. The estimated planet mass, if assumed to sit in a gap 59 au wide, aligns with a disk viscosity parameter $\alpha = 10^{-2}$ under the K. D. Kanagawa et al. (2016) model, or $\alpha = 10^{-4}$ under the S. Zhang et al. (2018) model. If we consider the lower bound of the measured gap width, approximately 46 au, based on the FWHM of the disk gap, the S. Zhang et al. (2018) model appears to more accurately capture the gap-opening efficiency of an embedded planet of this mass. Conversely, if the upper bound of 65 au (estimated from the K_s band) more accurately represents the gap width, again the S. Zhang et al. (2018) model with $\alpha = 10^{-4}$ offers an excellent match. Taken together, these results suggest that the disk viscosity might be well represented by at least $\alpha = 10^{-2}$ or higher.

7. Comparison with Other Young Planet-forming Systems

In the following we will put the WISPIT 2 system in context of similar young systems that either host a (candidate) planet embedded in the disk or that show a disk with multiple ring structures.

7.1. Systems with a Detected Protoplanet or Candidate

There are now several systems in the literature with resolved observations of the planet-forming environment and either direct or indirect detections of protoplanets or planet candidates. Of these, the most prominent is the PDS 70 system (M. Keppler et al. 2018; S. Y. Haffert et al. 2019) in which two gas giants with masses of 0.5–10 M_{Jup} and <5 M_{Jup} are located in the gap of a transition disk around a K-type star (A. Müller et al. 2018; D. Mesa et al. 2019; T. Stolker et al. 2020a; J. J. Wang et al. 2021). The size of the disk gap in the system (as measured from scattered light, near-infrared observations) is ∼54 au. The circumstellar disk consists of a single ring structure (M. Keppler et al. 2018) with possibly some outer spiral arms detected toward the disk ansae (S. Juillard et al. 2022) and has an outer extent of ∼100 au in scattered light. Compared with PDS 70, the disk around WISPIT 2 is significantly more extended (roughly by a factor of 3–4) and shows multiple concentric rings. The vertical aspect ratio of the disk around PDS 70 is 0.13 at 100 au (M. Keppler et al. 2018, based on J-band data), while the disk around WISPIT 2 is flatter, having an aspect ratio of 0.11. The embedded planet WISPIT 2b is located at ∼55 au, which is significantly farther out than is the case for either of the PDS 70 planets, which are located at 20.6 and 34.5 au for b and c, respectively (S. Y. Haffert et al. 2019). Given our photometric analysis, WISPIT 2b's mass appears to be close to the mass of PDS 70 b. We do not yet have a clear picture of the circumplanetary environment of WISPIT 2b. The observation of a significant Hα signal by L. M. Close et al. (2025b; companion Letter 2), seems to indicate the presence of a circumplanetary accretion disk, which is similar to the case of both PDS 70 planets.

In addition to the PDS 70 system, there are currently two strong candidates for directly detected, embedded protoplanets in the AB Aur system (T. Currie et al. 2022) as well as most recently in the HD 169142 system (R. Gratton et al. 2019; I. Hammond et al. 2023). Both of these orbit more-massive Herbig stars compared to the WISPIT 2 system. The main difference between both of these planet candidate detections and WISPIT 2b is that they both appear strongly embedded in local dust, with AB Aur b appearing as an extended source in the near-infrared and HD 169142 b showing a scattered stellar light spectrum (T. Currie et al. 2022; I. Hammond et al. 2023). Neither of these have significant direct Hα point-source emission detected, but AB Aur b may have evidence of weak variable, somewhat extended, Hα emission (B. P. Bowler et al. 2025). Of these two cases, the disk morphology with a bright inner ring and fainter outer rings of HD 169142 resembles most closely that of the WISPIT 2 system. However, we do not detect a significant polarized signal from the embedded planet position in WISPIT 2, which may suggest that the CPD is more depleted of dust than is the case for HD 169142. It may also be possible that the gap in the WISPIT 2 system is generally more depleted of material. An indication of this is that we see a signal in the inner disk ring that we speculate is

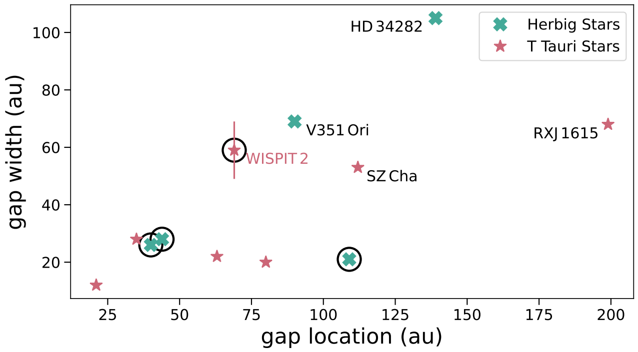

Figure 11. Full sample of all disk observations in near-infrared scattered light for which multiple rings were detected. We show the location and width of the widest gap in each system as given in the literature. When no specific gap widths were given, we used the difference between the peaks of adjoining rings as a measure for the gap width instead. Positional uncertainties are typically low and on the order of ∼1 au. We distinguish between T Tauri and Herbig stars. The systems with a similar or larger gap width as WISPIT 2 are labeled. The systems with a detected planet (WISPIT 2) or planet candidates (HD 169142, HD 163296, HD 97048) are indicated with a black circle around the marker.

the bottom side of the inner disk rim (see discussion in Appendix C). This structure should only be visible if the gap is almost devoid of small dust particles (J. George et al. 2025). The fact that the embedded planet in the WISPIT 2 system indeed presents as an unresolved point source with an $H - K_s$ color matching that of models of a young low-mass object (see Section 5) reinforces the interpretation that we are receiving mostly thermal emission from the planet location and not scattered light emission, and that the CPD is less pronounced in this case.

7.2. Multi-ringed Disks

While rings in disks are among the more common substructures detected in scattered light (see M. Benisty et al. 2023, for a recent review on disk demographics), multi-ringed disks are somewhat rarer. To the best of our knowledge, there are currently 12 systems known in the literature that show at least two rings in scattered light (see Appendix F). To compare the disk in the WISPIT 2 system with the larger population, we show in Figure 11 the widest gap width and location in each system as taken from the literature. The sample splits roughly evenly between low-mass T Tauri type stars and intermediate-mass Herbig Stars. Among the T Tauri star population, WISPIT 2 is among the disks with the widest gap between rings, with only the RX 1615 system showing a wider gap. However, morphologically these two systems present quite differently, whereas WISPIT 2 has relatively broad individual rings, the rings in RXJ 1615 are almost all very thin and radially not resolved (J. de Boer et al. 2016). The two Herbig systems with wider gaps than WISPIT 2 are V351 Ori and HD 34282. However, both of these objects show additional complex morphology possibly linked to large-scale spiral arms, which makes the interpretation of their gap structure challenging (J. de Boer et al. 2021; P. G. Valegård et al. 2024). Due to the significantly farther distance of these two systems compared to WISPIT 2, they are not well suited for the direct detection of planet thermal emission.

In addition to WISPIT 2, there are three other multi-ringed disks that have indications of embedded planet candidates: HD 169142, HD 163296, and HD 97048. While HD 169142 hosts a planet candidate also detected in the near-infrared (as discussed in Section 7.1), the planet candidates in HD 163296 and HD 97048 have been detected indirectly through local deviations of Keplerian motion of the disk gas at millimeter wavelengths (R. Teague et al. 2018; C. Pinte et al. 2019). This highlights that multi-ringed disk structures might indeed be the signpost of ongoing planet formation. However, all of these other systems are around more-massive Herbig stars and show significantly smaller gap widths. Consequently, the estimated planet masses are smaller than the inferred mass for WISPIT 2b, and in none of these cases has direct thermal emission been detected from the planet photosphere. Of particular note may be the comparison between the WISPIT 2 system and the HD 97048 system. By coincidence, both of these systems are viewed under a similar inclination and position angle. The overall morphology, with the large extent of scattered light signal as well as relatively broad individual rings, is very similar between them. It is then interesting in the context of the occurrence rate of massive planets that, of these two, the lower-mass T Tauri star has an embedded massive wide orbit super-Jupiter, while the Herbig star may only have a slightly lower-mass (2–3 M_{Jup}) embedded planet (C. Pinte et al. 2019).

8. Conclusions

In this study, we present the discovery of a directly imaged wide orbit (∼57 au) gas giant embedded in a multi-ringed disk around the young solar analog WISPIT 2. The astrometry of the planet relative to the central star across three observational epochs shows that the companion is inconsistent with a distant stationary background source. While additional high-precision astrometric measurements (e.g., with VLT/GRAVITY) are needed to constrain the dynamical mass of the planet–star system, the present data are compatible with a coplanar Keplerian orbit for WISPIT 2b inside the disk gap.

Photometric analysis places the companion between AMES-COND and AMES-DUSTY isochrones in color–magnitude space. Using the derived system age of $5.1^{+2.4}_{-1.3}$ Myr, we interpolated the absolute magnitudes of $M_{K_s} = 11.95^{+0.09}_{-0.09}$ mag and $M_H = 12.8^{+0.4}_{-0.3}$ mag to the AMES isochrone grids, and derived a companion mass of $4.9^{+0.9}_{-0.6}$ M_{Jup}—consistent with a planetary-mass object.

A detection of Hα emission (L. M. Close et al. 2025b, companion Letter 2) further confirms this planet and provides evidence of accretion, indicating the presence of a CPD. However, the lack of a polarized signal of WISPIT 2b may indicate that the CPD is more depleted of dust. The relatively blue $H - K_s$ color, apparent lack of dust in the surrounding disk gap, and the absence of polarized CPD emission leads us to conclude that CPD extinction is unlikely to significantly affect the derived photometry and the resulting mass estimate.

While the presence of embedded planets has long since been speculated to be a driver for substructure in ringed disks, the unambiguous detection of WISPIT 2b in the newly resolved disk surrounding WISPIT 2 provides us with the best laboratory to study planet–disk interaction in detail. Our preliminary analysis of the width of the disk gap in which the embedded planet resides, not only shows a general agreement with hydrodynamic models, but it also points us toward the possibility of using the embedded planet to measure the disk viscosity for the first time. This is a key parameter in the evolution of the planet-forming environment.

As the planet resides in the cleared gap and its mass is consistent with the modeled planet mass required to open such a gap, we argue that it likely formed in situ through core accretion and that there is no rapid migration on dynamical timescales. Future follow-up observations of WISPIT 2b with ALMA and JWST will enable studies of its atmosphere and the impact of the embedded planet on the disk's gas kinematics and surface density structure. This will allow us to calibrate ALMA observations of other embedded planet candidates, to unlock the full potential of this complementary technique. These future observations will also allow us to directly measure isotopologue ratios for CO in the disk to compare and contrast with spectroscopic isotopologue ratios measured directly from the planet (e.g., Y. Zhang et al. 2021, 2024; K. K. W. Hoch et al. 2025).

The discovery of WISPIT 2b embedded in the gap of a seemingly unperturbed disk demonstrates, for the first time, that wide-separation gas giants, discovered by direct imaging around older systems, can indeed form in situ. Thus, WISPIT 2b marks a promising starting point to study wide separation planets in time.

Acknowledgments

M.B. has received funding from the European Research Council (ERC) under the European Union's Horizon 2020 research and innovation program (PROTOPLANETS, grant agreement No. 101002188). R.T. was supported by JSPS KAKENHI grant Nos. JP25K07351 and JP25K01049. Part of this research was carried out at the Jet Propulsion Laboratory, California Institute of Technology, under a contract with the National Aeronautics and Space Administration (80NM0018D0004). The WISPIT team would like to thank Donna E. Keeley for her contributions to the survey program, and the anonymous reviewer for providing helpful feedback to this Letter.

Facility: VLT:Melipal.

Software: Python (https://www.python.org/), SciPy (P. Virtanen et al. 2020), NumPy (T. E. Oliphant 2006), Photutils (L. Bradley et al. 2016), Matplotlib (Astropy Collaboration et al. 2013), astropy (Astropy Collaboration et al. 2018).

Appendix A
Analysis of Stellar Parameters and Environs of WISPIT 2

The following appendix contains a detailed analysis of the stellar parameters and environs of WISPIT 2. Appendix A.1 discusses the reddening and extinction toward WISPIT 2. As it is not a member of a large young association, Appendix A.2 discusses membership to young stellar groups. The age of this group is analyzed in A.3 and compared to the age fit to WISPIT 2 based on its SED.

A.1. Interstellar Reddening toward WISPIT 2

The reported values for reddening and extinction by Gaia DR3 of $A_0 = 1.0855^{+0.0764}_{-0.0381}$, $A_G = 0.8601^{+0.0634}_{-0.0315}$, and $E(B_P - R_P) = 0.4706^{+0.0351}_{-0.0172}$ are unusually high for the region of WISPIT 2. In Figure 12, we plot the $E(B - V)$ reddening values from the recent analysis of E. Paunzen et al. (2024) for several stars within 1° of WISPIT 2 at a range of distances. The maximum interstellar reddening due to the full Galactic column of dust is estimated to be $E(B - V)_{\rm max} = 0.25$ mag from the E. F. Schlafly et al. (2010) updated to the D. J. Schlegel et al. (1998) IRAS dust maps, accessed via IRSA,[12] and indeed a distant B giant at $d \simeq$ 761 pc, HD 182411, has reddening $E(B - V) = 0.263$ in the E. Paunzen et al. (2024) catalog—the highest value within $0\overset{\circ}{.}8$ of WISPIT 2 . In Figure 12, the reddening values for the stars within 300 pc within 1° of WISPIT 2 in the E. Paunzen et al. (2024) catalog can be summarized by the following trends: (1) negligible reddening within ∼80 pc, due to the Local Bubble, and (2) a roughly linear trend between 80 pc $< d <$ 280 pc. At the distance of WISPIT 2 ($d \simeq 133$ pc), interpolation of the trend would predict interstellar reddening of $E(B - V) \simeq 0.043$ mag. This is consistent with the reddening estimate $E(B - V)$ quoted in the TESS Input Catalog ($E(B - V) = 0.0439 \pm 0.0279$ mag; K. G. Stassun et al. 2019), which are based upon the G. M. Green et al. (2018) Pan-STARRS 3D dust maps. This corresponds to $A_V = 0.1361 \pm 0.0865$ mag, which we adopt for our analysis of the SED.

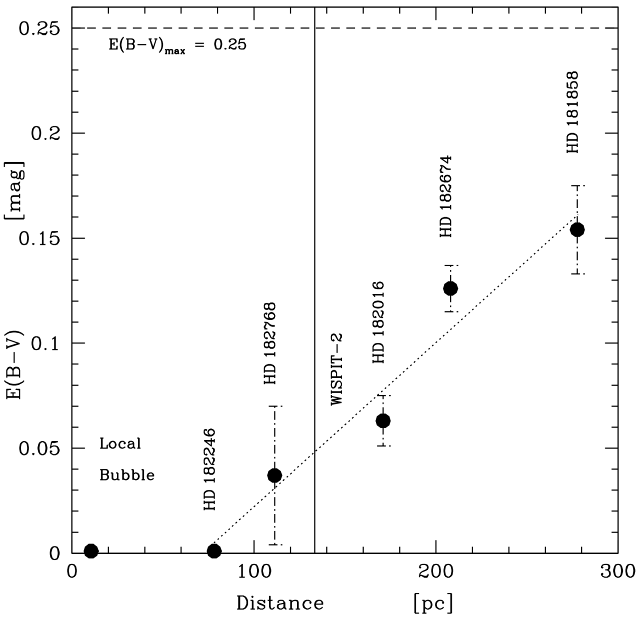

Figure 12. Distance vs. reddening $E(B - V)$ for stars within 1°, with distances based on Gaia DR3 parallaxes and reddening from E. Paunzen et al. (2024).

A.2. Memberships to Young Stellar Associations

Multiple authors have analyzed Gaia astrometric and photometric data and added WISPIT 2 to membership lists of recently identified young stellar groups, compiled in Table 5. M. Kounkel & K. Covey (2019) included WISPIT 2 in the membership list for their new group Theia 53, containing 44 members, and for which they estimated a mean age of log(age/yr) = 7.40 (25 Myr), mean parallax $\varpi = 7.394$ mas ($d = 135$ pc). R. M. P. Kerr et al. (2021) used HDBSCAN clustering algorithm on Gaia DR2 data and identified 27 "top level clusters" within 333 pc, including a sample of 30 associated stars (including WISPIT 2), which they designated "TLC 7" or "Aquila East."[13] R. M. P. Kerr et al. (2021) quoted a centroid position for the group at

---

[12] https://irsa.ipac.caltech.edu/applications/DUST/

[13] Use of "Aquila East" for the young stellar association TLC 7 should be deprecated as multiple studies refer to "Aquila East" as an active star formation region in the Aquila Rift complex (e.g., S. J. Park et al. 2012; E. Fiorellino et al. 2021).

Table 5
Mean Properties for Theia 53 Group and Its Aliases from Different Studies

References …	ID …	α (deg)	δ (deg)	$\mu_{\alpha*}$ (mas yr^{-1})	μ_{δ} (mas yr^{-1})	ϖ (mas)	$N_{\rm mem}$ …	log(age/yr) …	Lucida …
(1)	Theia 53	299.41	−7.14	…	…	7.39	44	7.40	57 Aql A
(2)	TLC-7	297.80	−9.00	8.5	−25.9	7.32 ± 0.35	30	7.305 ± 0.032	57 Aql A
(3)	OCSN 8	298.74	−8.18	9.73 ± 3.77	−25.44 ± 3.95	7.25 ± 0.36	60	7.95	57 Aql A
(4)	Theia 53/OCSN 8	298.75	−8.15	8.78 ± 3.93	−25.00 ± 4.14	7.70 ± 0.58	123	$7.553^{+0.255}_{-0.281}$	57 Aql A

Note. The ± values in proper motions and parallax are standard deviations, not standard errors.
References: (1) M. Kounkel & K. Covey (2019), (2) R. M. P. Kerr et al. (2021), (3) S. Qin et al. (2023), (4) E. L. Hunt & S. Reffert (2024).

$(\alpha, \delta) = (297\overset{\circ}{.}8, -9\overset{\circ}{.}0$; ICRS), $(\ell, b) = (31\overset{\circ}{.}6, -17\overset{\circ}{.}3)$, covering $12\overset{\circ}{.}2 \times 3\overset{\circ}{.}8$ degrees of sky, at distance $d = 136.6 \pm 6.5$ pc, and mean proper motion $(\mu_{\alpha*}, \mu_{\delta}) = (8.5, -25.9)$ mas yr^{-1}, which all compare well to WISPIT 2 . R. M. P. Kerr et al. (2021) also quoted a mean age of 20.2 ± 1.5 Myr.

S. Qin et al. (2023) identified a similar young group (OCSN 8) in the area, although did not alias it with Theia 53. They listed a membership of 60 member stars in Gaia DR3 for OCSN 8, with the brightest members being the bright B-type pair 57 Aql A and B. They estimated the mean parallax for OCSN 8 of $\varpi = 7.25 \pm 0.36$ mas (implying mean distance $d \simeq 138 \pm 7$ pc) and mean age log(age/yr) = 7.95, or 89 Myr. E. L. Hunt & S. Reffert (2024) detected this group again (entry 5493), cross-referencing it with both Theia 53 and OCSN 8, and increasing the membership list to 123 stars, among which is WISPIT 2 . They quoted a mean group parallax of $\varpi = 7.696$ (±0.581 mas st.dev; ±0.055 s.e.m.), implying a mean distance of $d = 130$ pc. They estimated Theia 53's age to be log (age/yr) = $7.55^{+0.26}_{-0.28}$ or $35.7^{+28.5}_{-17.0}$ Myr.

It is noteworthy that the T Tauri star BZ Sgr (PDS 101, IRAS 19558−1405, Gaia DR3 6878598726815263488) was included in the membership lists for both TLC-7 (R. M. P. Kerr et al. 2021) and OCSN 8 (S. Qin et al. 2023). BZ Sgr shows obvious youth indicators like strong Hα emission (EW(Hα) = –52 Å) and strong Li I absorption (EW (Li λ6707) = 0.33 Å). It is also situated next to the MBM 159 molecular cloud (L. Magnani et al. 1985), with a distance estimate of $d = 144$ pc (E. F. Schlafly et al. 2014). Previous characterizations of this group have a range of age estimates between ∼20 and ∼90 Myr, with the recent estimate by E. L. Hunt & S. Reffert (2024) including Gaia DR3 data for both Theia 53 and OCSN 8 defining the "state of the art." An updated age analysis of this group is included in Appendix A.3, but we note that further analysis is required to improve upon the group's age accuracy.

A.3. Age Classification of WISPIT 2

There are three comoving codistant stars that are on any of the membership lists for either Theia 53, OCSN 8, or TLC-7 with reported equivalent width measurement of lithium absorption lines. These targets are listed in Table 6. To estimate the age of the group, we used EAGLES, a software implementation of an empirical model that predicts the lithium equivalent width of a star as a function of age and effective temperature, as described in R. D. Jeffries et al. (2023). The results provide an upper limit of 13.6 Myr for the age of the group, as shown in Figure 13. A newer version of this software, EAGLES v2.0 (G. Weaver et al. 2024), implements an artificial neural network (ANN) model for the relationship between EW(Li), $T_{\rm eff}$, and age. This model is free from the constraints of an arbitrary analytical model, and provides better accuracy in reproducing the relationship between EW(Li) and its dispersion with age. It provides a cluster age of $11.1^{+5.9}_{-8.1}$ Myr, consistent with the upper limit provided by EAGLES, with the probability distribution in Figure 13 showing that it is indeed likely to be younger rather than older.

Table 6
Lithium Equivalent Widths and Effective Temperatures of Comoving Stars

ID	$T_{\rm eff}$ (K)	EW(Li) (mÅ)	References EW(Li)
UCAC4 416-129178	4135	490 ± 24.5	M. Žerjal et al. (2021)
TYC 5736-0649-1	5590	250 ± 12.5	C. A. O. Torres et al. (2006)
BZ Sgr (= UCAC2 27000662)	5280	400 ± 20.0	C. A. O. Torres et al. (2006)

Note. An error of 5% was assumed on the lithium equivalent width measurement.

Table 7
Mass and Age of WISPIT 2 from Stellar Isochrones

Model	Age (Myr)	Mass ($M_{\rm Jup}$)
BHAC15	$5.11^{+1.77}_{-0.61}$	$1.08^{+0.02}_{-0.07}$
PARSEC 1.2	$4.00^{+0.98}_{-0.91}$	$0.93^{+0.06}_{-0.07}$
SPOTS ($f = 0.17$)	$6.72^{+1.22}_{-1.10}$	$1.14^{+0.01}_{-0.04}$

While this provides an upper limit (EAGLES) or rough constraints (EAGLES v2.0) on the age of the young group to which WISPIT 2 likely belongs, it does not directly constrain the age of the star itself. To address this, we used the bolometric luminosity and effective temperature resulting from the VOSA SED fit and used VOSA to interpolate them to the BHAC15 stellar isochrone grid (I. Baraffe et al. 2015). The resulting age and mass are $5.11^{+1.77}_{-0.61}$ Myr and $1.08^{+0.02}_{-0.07}$ $M_{\odot}$, respectively. To investigate the systemic errors introduced by the evolutionary models, we have repeated this process for two other models: PARSEC 1.2 (A. Bressan et al. 2012) and SPOTS with a spot coverage fraction of $f = 0.17$ (G. Somers et al. 2020). Given the available SPOTS models, the choice of $f = 0.17$ is reasonable for T Tauri stars, which generally have spot coverage fractions between approximately 0.1 and 0.25 (e.g., J. Bouvier & C. Bertout 1989; M. Long et al. 2011; A. F. Lanza et al. 2016). As these models span a reasonable range around our preferred model (BHAC15; see Table 7 and Figure 14),

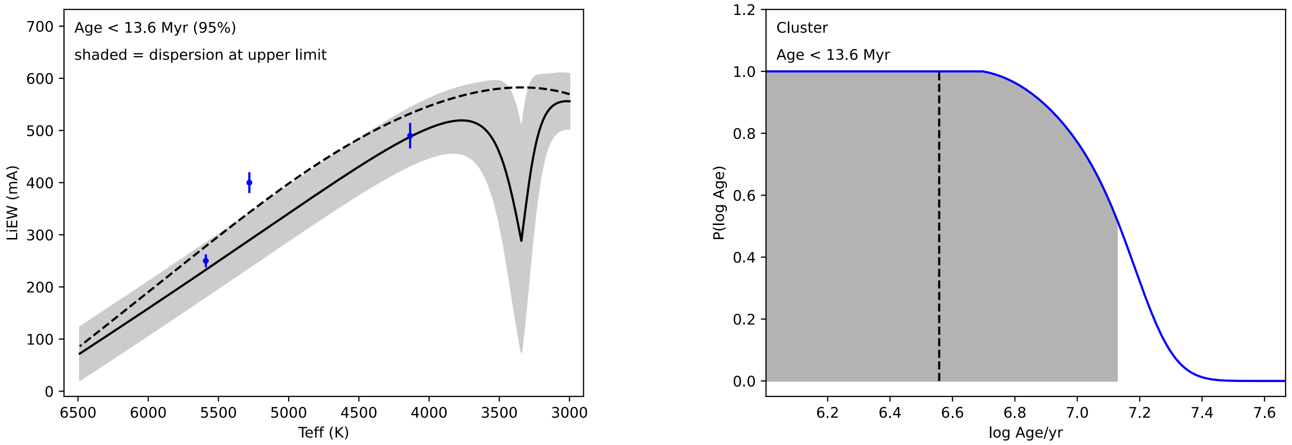

(a) Best-fit isochrone from EAGLES.

(b) Posterior probability distribution from EAGLES.

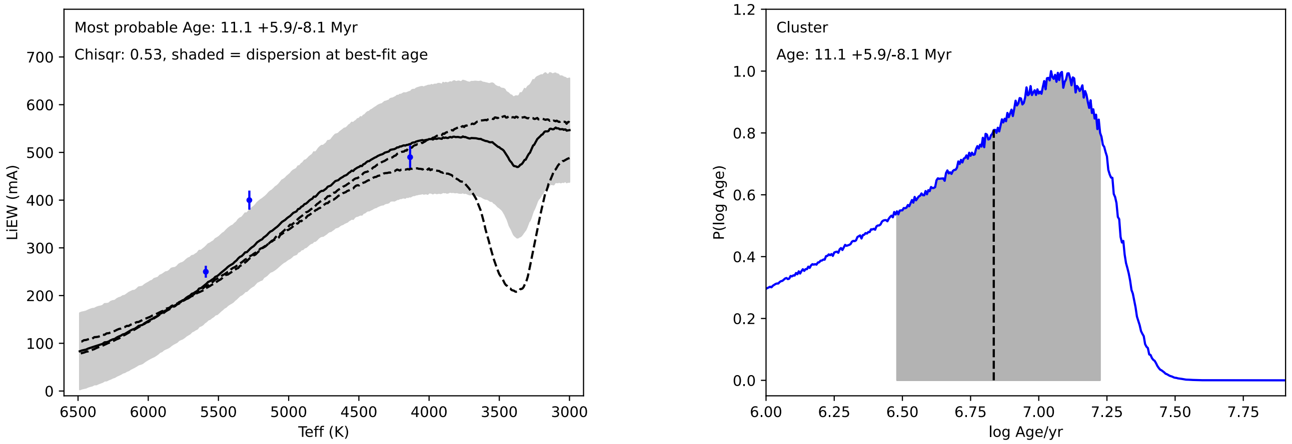

(c) Best-fit isochrone from EAGLES v2.0.

(d) Posterior probability distribution from EAGLES v2.0.

Figure 13. Results from fitting the age of the cluster using the EW(Li) and T_{eff} values listed in Table 6 with EAGLES (top panels) and EAGLES v2.0 (bottom panels).

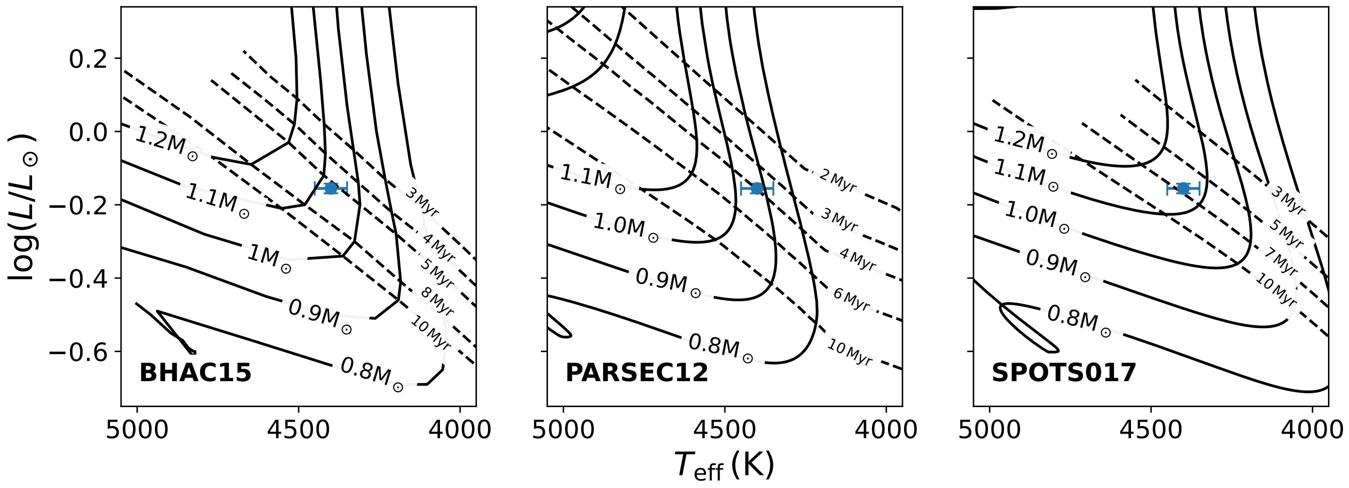

Figure 14. Stellar evolution isochrones for various masses (solid lines) and ages (dashed lines). The models are, from left to right, BHAC15, PARSEC 1.2, and SPOTS ($f = 0.17$). WISPIT 2 is indicated with a blue marker.

we adopt the derived age of 5.1 Myr as our fiducial value. We adjust the errors to account for systemic uncertainties due to the choice of evolutionary model by combining the model dependent variation in age with the BHAC15 fit errors in quadrature. This yields a final adopted age of $5.1^{+2.4}_{-1.3}$ Myr. Applying the same procedure to the mass results in a final adopted stellar mass of $1.08^{+0.06}_{-0.17}\,M_\odot$.

We note that the resulting age of $5.1^{+2.4}_{-1.3}$ Myr is consistent with the lower end of our derived age constraints for the Theia 53/OCSN 8/TLC-7 group.

Appendix B
Stokes *Q* and *U* Images

We show the Stokes Q and U images along with the derived Q_ϕ and U_ϕ images for the H- and K_s-band polarimetric observation epoch in Figures 15 and 16, respectively. Both observation epochs are flux calibrated, using the respective 2MASS H- and K_s-band magnitudes of the central star as reference. We show both observation epochs at the same absolute scale, demonstrating that the disk is significantly fainter in K_s-band compared to H-band polarized scattered light.

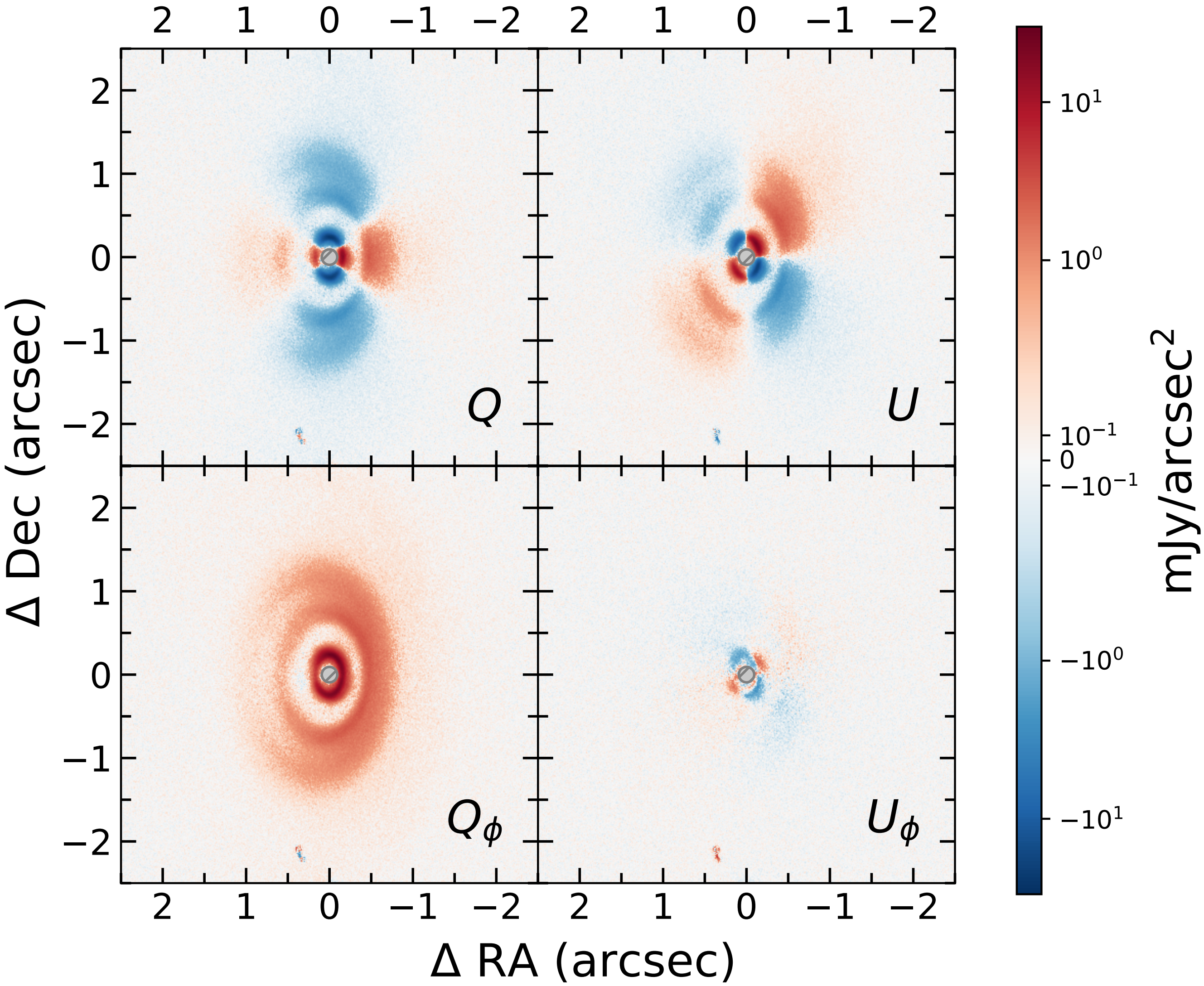

Figure 15. H-band Stokes Q and U and derived Q_ϕ and U_ϕ images of the WISPIT 2 disk. We note that polarized light observations are typically not sensitive to planet thermal emission, which is predominantly unpolarized. Consequently, the planet WISPIT 2b is not visible in these images.

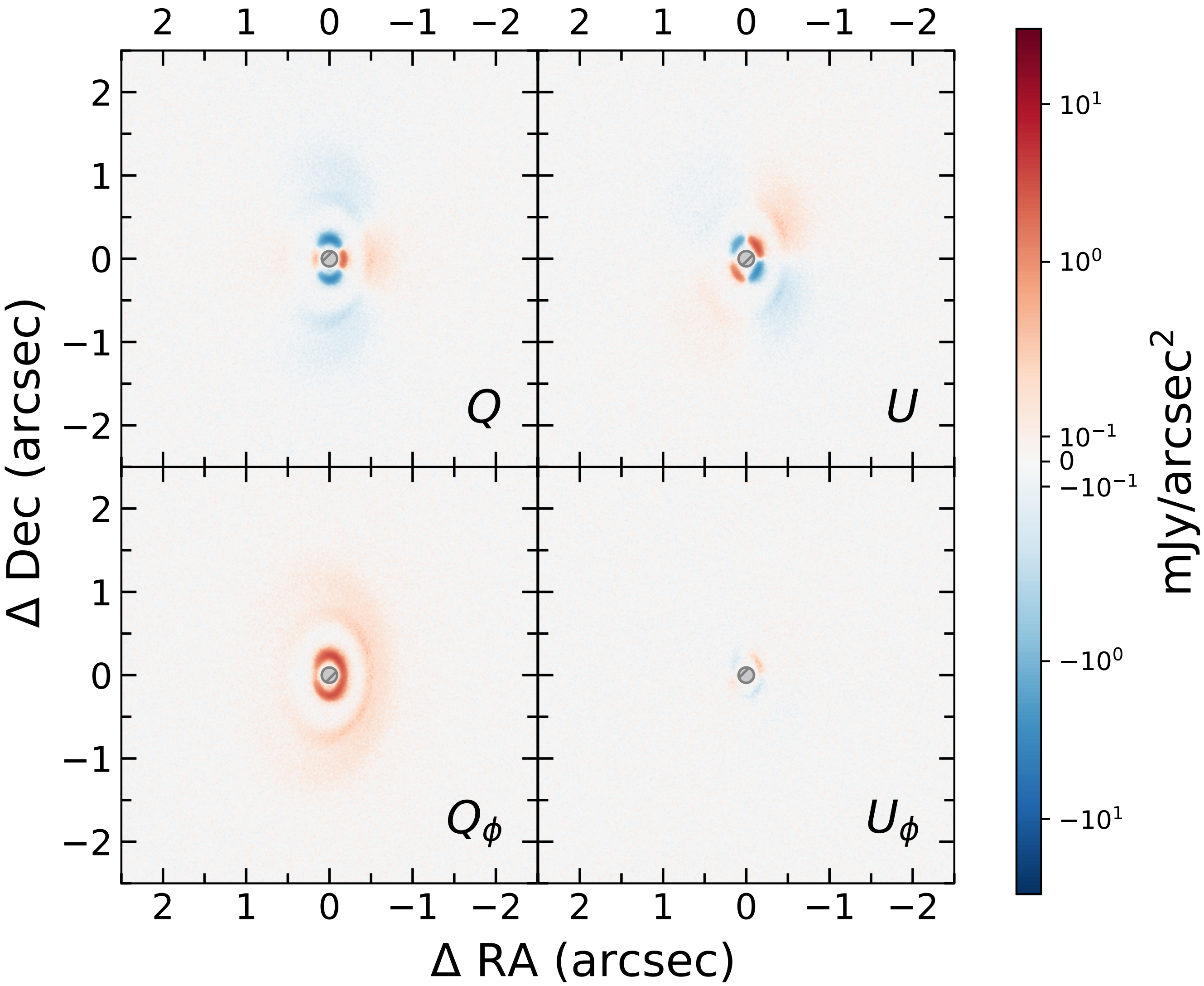

Figure 16. K_s-band Stokes Q and U and derived Q_ϕ and U_ϕ images of the WISPIT 2 disk. We note that polarized light observations are typically not sensitive to planet thermal emission, which is predominantly unpolarized. Consequently, the planet WISPIT 2b is not visible in these images.

Appendix C
Discussion of the Inner Disk Bottom Side

Scattered light images trace the upper vertical layers of the disk. This leads to an illuminated surface that is visible from our line of sight. If the disk is seen under moderate or large inclination, then it is possible to spot the dark lane, which demarcates the disk midplane and which appears dark, since no starlight reaches it to produce a scattered light signal. Following from the dark lane, there are some disks for which we can see the illuminated forward scattering rim of the disk bottom side. For a more detailed description of the appearance of scattered light disks, we refer the reader to the recent review by M. Benisty et al. (2023). The forward scattering rim of the disk bottom side has been detected for several disks. Archetypal examples would be the disk around the IM Lup system (H. Avenhaus et al. 2018) or more recently the disk in the PDS 111 system (A. Derkink et al. 2024). However, the disk bottom side is not detected for all inclined disks. This can be the case if there is an extended disk with low dust surface density obscuring our view along the line of sight. This is likely a common configuration, as we routinely find that the gas disks detected in tracers such as ^{12}CO with ALMA are significantly more extended than the disks seen in scattered light. If there is even a moderate amount of small dust particles still entrained in the disk gas, then it can easily make this diffuse outer region optically thick and thus obscure the view on the rim of the disk bottom side. This problem was recently investigated by George, Dominik & Ginski (2025, accepted). They found that in order to see the disk bottom side, the outer disk needs to be sharply truncated, possibly by a planetary or stellar companion or fly-by, so that little or no material remains to obscure the line of sight on the disk bottom side.

While the detection of the forward scattering rim of the disk bottom side is reasonably common on the outer edge of inclined disks, this has, to our knowledge, not been the case for the outer edge of an inner disk component seen through a gap inside the disk. To enable such a detection would mean that the gap itself needs to be near devoid of small dust particles, which would otherwise make the gap optically thick in the near-infrared. For the innermost disk ring (ring 3) in the WISPIT 2 system, we report the tentative detection of the forward scattering rim of the disk bottom side. We highlight the signal in question in Figure 17. We see evidence for the disk bottom side, both in the H-band polarized light image as

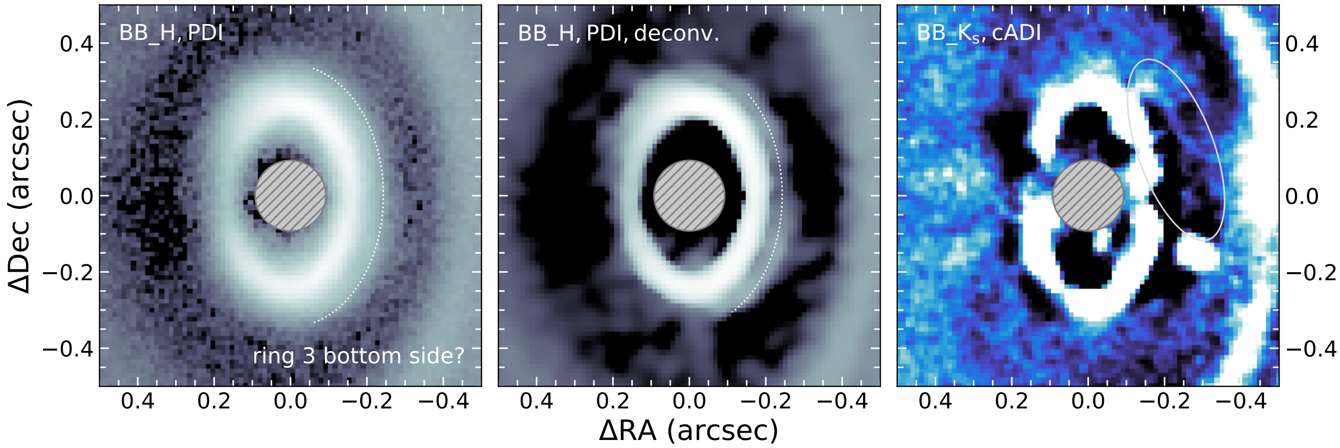

Figure 17. Zoom-in on the innermost disk ring (ring 3). We show polarized light Q_ϕ images in the gray color scheme in the left and middle panels and the total intensity cADI K_s-band image in the blue color scheme in the right panel. The middle panel shows the Q_ϕ image after image deconvolution was applied. The left and middle panels are displayed on a log scale due to the large dynamic range of the inner disk region, while the right panel is on a linear scale. The gray hashed circle in the image center marks the area covered by the coronagraphic mask. We indicate with dotted lines (left and middle panels) and with a solid encircling ellipse (right panel) the signature of the inner disk bottom side.

well as in the K_s-band total intensity image. For the H-band polarized light image, we can tell from Figure 17 (left panel) that the bright ridge of the ring has an extended "halo" in a crescent shape centered along the disk minor axis toward the west. Such a crescent shape would indeed be the expected morphology of the forward scattering rim of the disk bottom side. To highlight this feature, we performed an image deconvolution using the Adaptive Image Deconvolution Algorithm (E. F. Y. Hom et al. 2007) Python package. We used a flux calibration image (in which no disk signal was detected due to the short integration time) as realization of the instrumental PSF as input for the deconvolution. A similar analysis was recently performed to highlight the narrow gaps in the PDS 111 system by A. Derkink et al. (2024). The resulting deconvolved image is shown in Figure 17 (middle panel). The crescent-shaped signal is pronounced and appears distinct for the main ring ridge.

We also tentatively detect a signature of the disk bottom side in the K_s-band classical ADI image shown in Figure 17 (right panel). The ADI procedure effectively acts as a high pass filter, highlighting sharp disk structures while self-subtracting more diffuse signal (see, e.g., the discussion in J. Milli et al. 2012; L. M. Stapper & C. Ginski 2022). In the cADI image, we tentatively see a faint crescent-shaped ridge again to the West of the main ring (highlighted by the elliptical aperture). This signal is in line with what might be expected from the ridge of the visible disk bottom side.

While our interpretation of this signal is strengthened by its detection in two independent data sets and reductions, we do note that we do not see a clear detection of the separating dark lane that one might expect between the forward scattering rims of the disk top and bottom sides. This is likely due to too low spatial resolution of our observations. Based on our geometric fitting of the inner ring (ring 3), we find that it has a height of the scattering surface of 1.7 au. This means the dark lane separating the disk top and bottom sides should have a thickness of 3.4 au. Given the distance and inclination of the system, this translates to a thickness of 18 mas, i.e., less than half of the resolution element we have in the H band. Thus, our nondetection of the disk midplane signature is consistent with our interpretation. To solidify this interpretation, follow-up observations in the optical with SPHERE/ZIMPOL in the R or V band might be able to resolve the disk midplane.

Appendix D
Gaussian Fitting Routine for Astrometric Measurement

To obtain astrometric measurements, we fitted the `Astropy` (Astropy Collaboration et al. 2013, 2018, 2022) 2D Gaussian model to the approximate position of the companion. We used the `TRFLSQFitter`, a Trust Region Reflective algorithm with bound constraints and least-squares statistics. The center of the Gaussian fit was constrained to lie within 3 pixels (i.e., a 6×6 pixel region) of the manually estimated (x, y) position. Additionally, to ensure that the fitted FWHM is consistent with that of SPHERE/IRDIS observations, we constrained the standard deviation of the Gaussian be within 2.0 pixels of the median PSF standard deviation in the H band. This median PSF was constructed from YSES observations—all contributing observations are listed in Table 11 in Appendix I. These constraints were implemented to ensure that only the physical planet signal was fitted. However, to avoid biasing the results with the imposed bounds, we removed a fit from the results if a bound of a constraint was touched, even if that fit formally converged.

Appendix E
Geometric Fitting Results Table

In Table 8, we present the results of our ellipse fitting approach (discussed in Section 4) to the individual substructures. As we fit each structure individually, we obtain a small range of disk inclinations and position angles. Here, the position angle follows the convention that it is measured from the north in direction of east (counterclockwise) toward the disk major axis on the disk near side (see Figure 18). This could indicate in principle that there are small relative misalignments between different disk structures. We note that these differences in inclination and position angle appear to be somewhat consistent between the H- and K_s-band images; e.g., among the rings 1–3, ring 1 has in both cases the largest measured inclination and ring 2 has the smallest. However, this result is of very low significance at this stage, and detailed

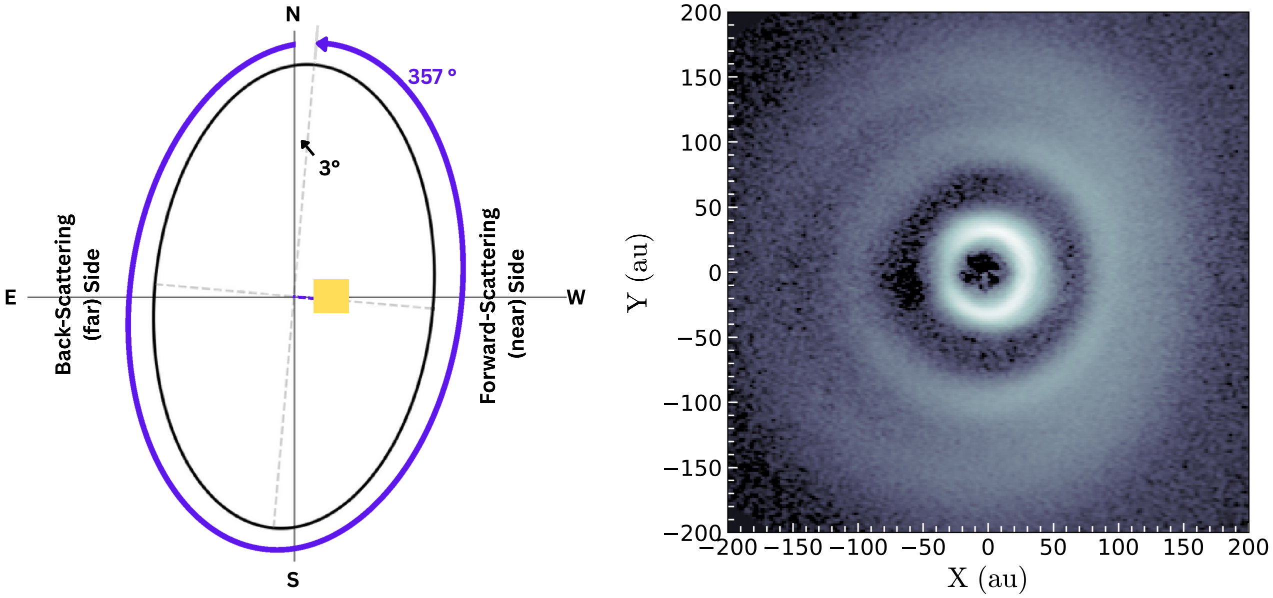

(a) Position angle convention.

(b) De-projected disk.

Figure 18. Panel (a): definition of the PA, measured counterclockwise from north to east. In this convention, the PA is measured from north to the major axis and contains the forward scattering side, corresponding to a PA of 357°in this diagram. Panel (b): image of the disk de-projected using the height and inclination measurements extracted from individual rings following this convention, with angular size on sky translated to astronomical unit.

Table 8
Results of the Geometric Fitting of WISPIT 2

		Separation (au)	Height (au)	Aspect Ratio (h/r)	Inclination (deg)	Position Angle (deg)
H-band	Ring 0	316.361 ± 4.499	76.083 ± 6.315	0.240 ± 0.030	43.618 ± 1.543	357.811 ± 1.556
	Ring 1	163.554 ± 2.928	24.048 ± 1.148	0.147 ± 0.007	45.397 ± 1.074	356.511 ± 1.311
	Ring 2	96.729 ± 0.634	10.444 ± 0.623	0.108 ± 0.006	41.797 ± 0.564	357.097 ± 1.548
	Gap 3	68.989 ± 0.600	4.098 ± 0.665	0.059 ± 0.010	44.185 ± 0.757	0.472 ± 0.917
	Ring 3	38.441 ± 0.078	1.700 ± 0.154	0.044 ± 0.004	44.953 ± 0.393	1.540 ± 0.279
K_s-band	Ring 1	156.298 ± 1.763	17.934 ± 2.731	0.115 ± 0.018	47.517 ± 1.266	356.816 ± 1.496
	Ring 2	102.745 ± 1.363	6.621 ± 1.576	0.064 ± 0.015	42.642 ± 1.272	359.343 ± 4.458
	Gap 3	68.005 ± 1.449	2.585 ± 1.351	0.038 ± 0.020	49.322 ± 1.662	0.828 ± 2.871
	Ring 3	37.224 ± 0.125	1.093 ± 0.485	0.029 ± 0.013	43.972 ± 0.876	0.243 ± 0.482

Note. Results for fitting the rings present in our data. Further details on the different fitting methods are found in Section 4. Ring 0 was not detectable in the K_s band.

modeling of the disk (beyond the scope of this study) might be needed to verify such a small misalignment or warp in the disk. In Figure 18 we show the disk de-projected using our height measurements as well as the inclination and major axis position angle. We find that the de-projection shows reasonable circular rings as expected for a noneccentric disk.

Appendix F
Multi-ringed Disk Population

To put the WISPIT 2 system in context of previous observations of planet-forming disks, we have assembled from the literature all disks that show a similar morphology, i.e., a multiple ring structure in near-infrared scattered light. We note that we, for now, exclude systems with multiple rings detected with submillimeter observations, unless they also have multiple rings detected in scattered light. This is mainly due to the fact that we do not currently have submillimeter observations of the WISPIT 2 system and thus cannot directly compare to other such observations. In Table 9 we give the full literature sample of such disks, the reference publication, as well as the values for the width and location of the widest gap in the system used for Figure 11.

Table 9
Literature Sample of Multi-ringed Scattered Light Disks

System Name	References	Gap Width (au)	Gap Location (au)
HD 163296	C. A. Grady et al. (2000), J. D. Monnier et al. (2017)	26	40
HD 169142	S. P. Quanz et al. (2013)	28	44
HD 34282	J. de Boer et al. (2021)	105	139
HD 34700	J. D. Monnier et al. (2019), G. Columba et al. (2024)	⋯	⋯
HD 97048	C. Ginski et al. (2016)	21	109
PDS 111	A. Derkink et al. (2024)	22	63
RX J1615.3 −3255	J. de Boer et al. (2016)	68	199
SZ Cha	C. Ginski et al. (2024)	53	112
TW Hya	R. van Boekel et al. (2017)	20	80
V 351 Ori	P. G. Valegård et al. (2024)	69	90
V 4046 Sgr	H. Avenhaus et al. (2018)	12	21
WRAY 15-788	A. J. Bohn et al. (2019)	28	35

Note. As reference, we always give the first observation in which the multi-ringed substructure was detected and/or measured in detail. In cases where subsequent substructure was detected over the course of time, we give the detection of the first ring-like structure and the first paper in which then a second ring was discovered. Gap width and location refer to the widest detected gap in the system. If no specific center gap location was fitted in the reference literature, then we refer to the geometric center between the two adjacent rings as gap location. We only include Class II disks in this sample. For the HD 34700 system, we do not give a gap width and location, as the disk structure is strongly asymmetric.

Appendix G
Constructing the Composite Image

We show the page-wide version of Figure 1 in Figure 19. This composite figure is constructed using the polarized-light H- and K_s-band images for the disk signal and masked versions of the 2023 RDI H and 2025 cADI K_s-band total intensity images for the planet. The polarized light images are not sensitive to the thermal emission of the planet (since thermal emission is unpolarized), and thus, the planet is not visible in these images. Conversely, these are the images that best highlight the disk structure without any morphological artifacts introduced by, e.g., ADI. The H and K_s images were taken with the same single-exposure settings (64 s). We use the H-band image for the blue channel of the image and the K_s-band image for the red channel of the image. Since we do not have a third wavelength for the disk, at this point, we use the average of the H- and K_s-band data for the green channel. The image is displayed on a logarithmic color scale to highlight the full disk features and extend. For the planet signal, we used a similar approach, i.e., we used the H-band data for the blue image channel, the average of the H and K_s band for the green channel, and the K_s-band data for the red channel. To suppress the somewhat distorted disk signal in these images, we cut out a small square area around the planet in the H-band image and an annulus centered on the disk gap for the K_s-band image. Since the underlying K_s-band data for the polarized image of the disk and total intensity image of the disk are identical, the relative position of the planet to the disk is accurate. Since the H-band total intensity image of the planet was taken about 2 yr prior to the K_s-band data, the planet showed significant orbital motion (as we discuss in Section 5.1). To avoid a smeared appearance of the planet for the purpose of this illustrative figure, we thus centered the 2023 H-band observation of the planet on the same position as the 2025 K_s-band observation. The figure therefore depicts the accurate position of the planet relative to the disk and the central star as of 2025 April 26.

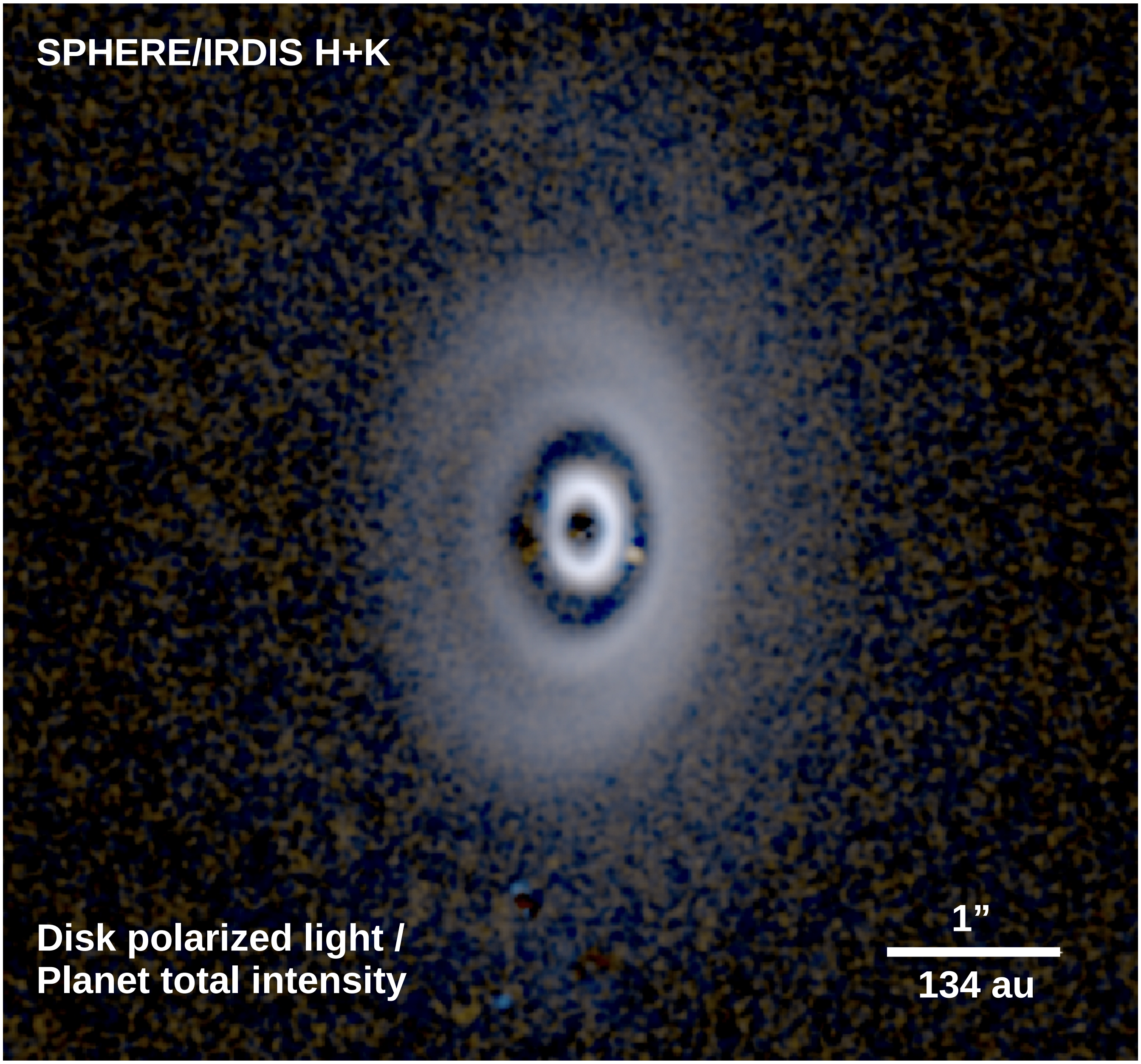

Figure 19. SPHERE/IRDIS multiband image of the WISPIT 2 system. The H-band Q_ϕ image was added as the blue channel and the median combination of the H-band and K_s-band Q_ϕ images was added as the green channel. The red channel is a combination of the K_s-band Q_ϕ image and the K_s-band cADI image in which we masked all but the gap containing the thermal emission from WISPIT 2b .

Appendix H
Reference Library for *H*-band RDI Reduction

In Table 10 we provide all observations that were used for the RDI library for PCA-based RDI processing of the WISPIT 2 H-band data taken in 2023 and 2024. This library is a subset of all YSES observations, filtered to remove low-quality observations, misaligned frames, frames with sources in the field of view, and close stellar binaries. The resulting library consists of 340 frames of which, for each observation, the 275 frames with the highest correlation were selected based on MSE.

Table 10
Observations Used for Constructing the H Band RDI Reference Library

Target Name	Archive Name	Observation Date
ASAS J114452-6438.9	2MASS J11445217-6438548	2018-05-14
ASAS J114452-6438.9	2MASS J11445217-6438548	2023-04-20
1RXS J114519.6-574925	2MASS J11452016-5749094	2018-05-14
1RXS J114542.7-573928	2MASS J11454278-5739285	2018-06-05
1RXS J114542.7-573928	2MASS J11454278-5739285	2019-01-13
1RXS J114542.7-573928	2MASS J11454278-5739285	2023-04-20
1RXS J120652.1-504448	2MASS J12065276-5044463	2017-04-02
1RXS J121010.3-485538	2MASS J12101065-4855476	2017-04-18
CD-57 4328	2MASS J12113142-5816533	2018-12-22
CD-57 4328	2MASS J12113142-5816533	2019-02-18
PM J12160-5614	2MASS J12160114-5614068	2018-12-27
RX J1216.6-7007A	2MASS J12164023-7007361	2018-12-23
RX J1216.6-7007A	2MASS J12164023-7007361	2019-02-15
RX J1216.6-7007A	2MASS J12164023-7007361	2023-12-21
CPD-64 1859	2MASS J12192161-6454101	2023-06-17
RX J1220.0-5018A	2MASS J12195938-5018404	2018-12-30
RX J1220.0-5018A	2MASS J12195938-5018404	2023-06-17
CD-47 7559	2MASS J12220430-4841248	2017-04-18
ASAS J122648-5214.8	2MASS J12264842-5215070	2018-12-30
ASAS J122648-5214.8	2MASS J12264842-5215070	2023-05-28
RX J1230.5-5222	2MASS J12302957-5222269	2018-12-30
RX J1230.5-5222	2MASS J12302957-5222269	2022-03-30
CPD-56 5307	2MASS J12333381-5714066	2019-01-01
CPD-56 5307	2MASS J12333381-5714066	2019-01-14
CPD-56 5307	2MASS J12333381-5714066	2023-05-28
CPD-50 5313	2MASS J12361767-5042421	2018-12-30
2MASS J12374883-5209463	2MASS J12374883-5209463	2018-12-30
2MASS J12374883-5209463	2MASS J12374883-5209463	2023-07-14
1RXS J123834.9-591645	2MASS J12383556-5916438	2019-01-03
1RXS J123834.9-591645	2MASS J12383556-5916438	2019-01-12
1RXS J123834.9-591645	2MASS J12383556-5916438	2023-07-14
CD-56 4581	2MASS J12393796-5731406	2017-06-17
CD-51 6900	2MASS J12404664-5211046	2018-04-30
CD-51 6900	2MASS J12404664-5211046	2023-05-30
ASAS J124547-5411.0	2MASS J12454884-5410583	2018-04-30
HD 111227	2MASS J12480778-4439167	2017-04-18
1RXS J124830.1-594449	2MASS J12483152-5944493	2023-08-07
V1257 Cen	2MASS J12505143-5156353	2019-01-12
CPD-52 6110	2MASS J13015069-5304581	2019-01-08
ASAS J130550-5304.2	2MASS J13055087-5304181	2018-06-11
ASAS J130550-5304.2	2MASS J13055087-5304181	2018-07-05
ASAS J130550-5304.2	2MASS J13055087-5304181	2022-04-02
CD-51 7268	2MASS J13064012-5159386	2018-04-30
CD-51 7268	2MASS J13064012-5159386	2023-06-15
2MASS J13065439-4541313	2MASS J13065439-4541313	2018-04-08
2MASS J13065439-4541313	2MASS J13065439-4541313	2023-07-08
UCAC2 12444765	2MASS J13095880-4527388	2018-05-01
ASAS J131033-4816.9	2MASS J13103245-4817036	2018-05-01
2MASS J13121764-5508258	2MASS J13121764-5508258	2017-08-31
2MASS J13121764-5508258	2MASS J13121764-5508258	2018-05-15
UNSW-V 514	2MASS J13174687-4456534	2018-05-28
2MASS J13334410-6359345	2MASS J13334410-6359345	2017-07-05
2MASS J13334410-6359345	2MASS J13334410-6359345	2023-06-16
CD-41 7947	2MASS J13343188-4209305	2017-04-02
CD-41 7947	2MASS J13343188-4209305	2023-08-07
TYC 8265-229-1	2MASS J13354082-4818124	2017-04-02
TYC 7800-858-1	2MASS J13380596-4344564	2017-04-02
CD-56 4581	CD-56 4581	2024-06-13
HD 304428	HD 304428	2024-06-10
RX J1216.6-7007A	TYC 9231-1185-1	2024-06-10
UCAC4 186-087394	UCAC4 186-087394	2024-06-13

Appendix I
Median PSFs

Table 11 contains all observations used to create the normalized median flux PSF in the *H* band. Here, "Target Name" denotes the commonly used designation for the source, and "Archive Name" corresponds to the name it is registered under in the ESO Science Archive Facility.

Table 11
Flux Observations Used for Constructing the Median *H*-band PSF

Target Name	Archive Name	Observation Date
1RXS J114519.6-574925	2MASS J11452016-5749094	2018-05-14
1RXS J114542.7-573928	2MASS J11454278-5739285	2019-01-13
1RXS J114542.7-573928	2MASS J11454278-5739285	2023-04-20
1RXS J121010.3-485538	2MASS J12101065-4855476	2017-04-18
1RXS J123834.9-591645	2MASS J12383556-5916438	2019-01-03
1RXS J123834.9-591645	2MASS J12383556-5916438	2019-01-12
1RXS J123834.9-591645	2MASS J12383556-5916438	2023-07-14
1RXS J124830.1-594449	2MASS J12483152-5944493	2023-08-07
2MASS J12374883-5209463	2MASS J12374883-5209463	2018-12-30
2MASS J12374883-5209463	2MASS J12374883-5209463	2023-07-14
2MASS J13065439-4541313	2MASS J13065439-4541313	2018-04-08
2MASS J13065439-4541313	2MASS J13065439-4541313	2023-07-08
2MASS J13121764-5508258	2MASS J13121764-5508258	2018-05-15
2MASS J13334410-6359345	2MASS J13334410-6359345	2023-06-16
ASAS J114452-6438.9	2MASS J11445217-6438548	2018-05-14
ASAS J114452-6438.9	2MASS J11445217-6438548	2023-04-20
ASAS J122648-5214.8	2MASS J12264842-5215070	2018-12-30
ASAS J122648-5214.8	2MASS J12264842-5215070	2023-05-28
ASAS J124547-5411.0	2MASS J12454884-5410583	2018-04-30
ASAS J130550-5304.2	2MASS J13055087-5304181	2022-04-02
ASAS J131033-4816.9	2MASS J13103245-4817036	2018-05-01
CD-41 7947	2MASS J13343188-4209305	2023-08-07
CD-47 7559	2MASS J12220430-4841248	2017-04-18
CD-51 6900	2MASS J12404664-5211046	2018-04-30
CD-51 6900	2MASS J12404664-5211046	2023-05-30
CD-51 7268	2MASS J13064012-5159386	2018-04-30
CD-51 7268	2MASS J13064012-5159386	2023-06-15
CD-57 4328	2MASS J12113142-5816533	2018-12-22
CD-57 4328	2MASS J12113142-5816533	2019-02-18
CPD-50 5313	2MASS J12361767-5042421	2018-12-30
CPD-52 6110	2MASS J13015069-5304581	2019-01-08
CPD-56 5307	2MASS J12333381-5714066	2019-01-01
CPD-56 5307	2MASS J12333381-5714066	2019-01-14
CPD-56 5307	2MASS J12333381-5714066	2023-05-28
CPD-64 1859	2MASS J12192161-6454101	2023-06-17
PM J12160-5614	2MASS J12160114-5614068	2018-12-27
RX J1216.6-7007A	2MASS J12164023-7007361	2018-12-23
RX J1216.6-7007A	2MASS J12164023-7007361	2019-02-15
RX J1216.6-7007A	2MASS J12164023-7007361	2023-12-21
RX J1216.6-7007A	TYC 9231-1185-1	2024-06-10
RX J1220.0-5018A	2MASS J12195938-5018404	2018-12-30
RX J1220.0-5018A	2MASS J12195938-5018404	2023-06-17
RX J1230.5-5222	2MASS J12302957-5222269	2018-12-30
RX J1230.5-5222	2MASS J12302957-5222269	2022-03-30
UCAC2 12444765	2MASS J13095880-4527388	2018-05-01
UCAC4 186-087394	UCAC4 186-087394	2024-06-13
UNSW-V 514	2MASS J13174687-4456534	2018-05-28
V1257 Cen	2MASS J12505143-5156353	2019-01-12

ORCID iDs

Richelle F. van Capelleveen https://orcid.org/0009-0002-6729-646X
Christian Ginski https://orcid.org/0000-0002-4438-1971
Matthew A. Kenworthy https://orcid.org/0000-0002-7064-8270
Jake Byrne https://orcid.org/0009-0002-6096-9617
Chloe Lawlor https://orcid.org/0009-0001-0368-1062
Dan McLachlan https://orcid.org/0009-0002-4783-6529
Eric E. Mamajek https://orcid.org/0000-0003-2008-1488
Tomas Stolker https://orcid.org/0000-0002-5823-3072
Myriam Benisty https://orcid.org/0000-0002-7695-7605
Alexander J. Bohn https://orcid.org/0000-0003-1401-9952
Laird M. Close https://orcid.org/0000-0002-2167-8246
Carsten Dominik https://orcid.org/0000-0002-3393-2459
Sebastiaan Haffert https://orcid.org/0000-0001-5130-9153
Rico Landman https://orcid.org/0000-0002-7261-8083
Jie Ma https://orcid.org/0000-0003-3583-6652
Ignas Snellen https://orcid.org/0000-0003-1624-3667
Ryo Tazaki https://orcid.org/0000-0003-1451-6836
Nienke van der Marel https://orcid.org/0000-0003-2458-9756
Lukas Welzel https://orcid.org/0009-0008-8810-6577
Yapeng Zhang https://orcid.org/0000-0003-0097-4414

References

Allard, F., Hauschildt, P. H., Alexander, D. R., Tamanai, A., & Schweitzer, A. 2001, ApJ, 556, 357
Allard, F., Homeier, D., Freytag, B., Schaffenberger, W., & Rajpurohit, A. S. 2013, MSAIS, 24, 128
Amara, A., & Quanz, S. P. 2012, MNRAS, 427, 948
Astropy Collaboration, Price-Whelan, A. M., Lim, P. L., et al. 2022, ApJ, 935, 167
Astropy Collaboration, Price-Whelan, A. M., Sipőcz, B. M., et al. 2018, AJ, 156, 123
Astropy Collaboration, Robitaille, T. P., Tollerud, E. J., et al. 2013, A&A, 558, A33
Avenhaus, H., Quanz, S. P., Garufi, A., et al. 2018, ApJ, 863, 44
Bae, J., Isella, A., Zhu, Z., et al. 2023, in ASP Conf. Ser. 534, Protostars and Planets VII, ed. S. Inutsuka et al. (San Francisco, CA: ASP), 423
Bae, J., Zhu, Z., & Hartmann, L. 2017, ApJ, 850, 201
Bailer-Jones, C. A. L., Rybizki, J., Fouesneau, M., Demleitner, M., & Andrae, R. 2021, AJ, 161, 147
Baraffe, I., Homeier, D., Allard, F., & Chabrier, G. 2015, A&A, 577, A42
Bayo, A., Rodrigo, C., Barrado Y Navascués, D., et al. 2008, A&A, 492, 277
Benisty, M., Bae, J., Facchini, S., et al. 2021, ApJL, 916, L2
Benisty, M., Dominik, C., Follette, K., et al. 2023, in ASP Conf. Ser. 534, Protostars and Planets VII, ed. S. Inutsuka et al. (San Francisco, CA: ASP), 605
Beuzit, J. L., Vigan, A., Mouillet, D., et al. 2019, A&A, 631, A155
Bianchi, L., Herald, J., Efremova, B., et al. 2011, Ap&SS, 335, 161
Blunt, S., Nielsen, E. L., De Rosa, R. J., et al. 2017, AJ, 153, 229
Blunt, S., Wang, J. J., Angelo, I., et al. 2020, AJ, 159, 89
Bohn, A. J., Ginski, C., Kenworthy, M. A., et al. 2021, A&A, 648, A73
Bohn, A. J., Kenworthy, M. A., Ginski, C., et al. 2019, A&A, 624, A87
Boss, A. P. 1997, Sci, 276, 1836
Bouvier, J., & Bertout, C. 1989, A&A, 211, 99
Bowler, B. P., Zhou, Y., Biddle, L. I., et al. 2025, AJ, 169, 258
Bradley, L., Sipocz, B., Robitaille, T., et al. 2016, Photutils: Photometry Tools, Astrophysics Source Code Library, ascl:1609.011
Bressan, A., Marigo, P., Girardi, L., et al. 2012, MNRAS, 427, 127
Chabrier, G., Baraffe, I., Allard, F., & Hauschildt, P. 2000, ApJ, 542, 464
Chambers, K. C., Magnier, E. A., Metcalfe, N., et al. 2016, arXiv:1612.05560
Christiaens, V., Cantalloube, F., Casassus, S., et al. 2019, ApJL, 877, L33
Close, L. M., Males, J. R., Li, J., et al. 2025a, AJ, 169, 35
Close, L. M., van Cappelleveen, R. F., Weible, G., et al. 2025b, ApJL, 990, L9
Columba, G., Rigliaco, E., Gratton, R., et al. 2024, A&A, 681, A19
Currie, T., Marois, C., Cieza, L., et al. 2019, ApJL, 877, L3
Currie, T., Lawson, K., Schneider, G., et al. 2022, NatAs, 6, 751
Cutri, R. M., Skrutskie, M. F., van Dyk, S., et al. 2003, 2MASS All Sky Catalog of Point Sources (Greenbelt, MD: NASA)
Cutri, R. M., Wright, E. L., Conrow, T., et al. 2012, Explanatory Supplement to the WISE All-Sky Data Release Products
Dawson, R. I., & Fabrycky, D. C. 2010, ApJ, 722, 937
de Boer, J., Ginski, C., Chauvin, G., et al. 2021, A&A, 649, A25
de Boer, J., Langlois, M., van Holstein, R. G., et al. 2020, A&A, 633, A63
de Boer, J., Salter, G., Benisty, M., et al. 2016, A&A, 595, A114
Derkink, A., Ginski, C., Pinilla, P., et al. 2024, A&A, 688, A149
Dohlen, K., Langlois, M., Saisse, M., et al. 2008, Proc. SPIE, 7014, 70143L
Dupuy, T. J., Liu, M. C., Allers, K. N., et al. 2018, AJ, 156, 57
Epchtein, N., Deul, E., Derriere, S., et al. 1999, A&A, 349, 236
Fiorellino, E., Elia, D., André, P., et al. 2021, MNRAS, 500, 4257
Fitzpatrick, E. L. 1999, PASP, 111, 63
Follette, K. B., Rameau, J., Dong, R., et al. 2017, AJ, 153, 264
Gaia Collaboration, Vallenari, A., Brown, A. G. A., et al. 2023, A&A, 674, A1
Gapp, C., Evans-Soma, T. M., Barstow, J. K., et al. 2025, AJ, 169, 341
George, J., Dominik, C., & Ginski, C. 2025, A&A, 699, A254
Ginski, C., Facchini, S., Huang, J., et al. 2021, ApJL, 908, L25
Ginski, C., Garufi, A., Benisty, M., et al. 2024, A&A, 685, A52
Ginski, C., Stolker, T., Pinilla, P., et al. 2016, A&A, 595, A112
Goffo, E., Gandolfi, D., Egger, J. A., et al. 2023, ApJL, 955, L3
Grady, C. A., Devine, D., Woodgate, B., et al. 2000, ApJ, 544, 895
Gratton, R., Ligi, R., Sissa, E., et al. 2019, A&A, 623, A140
Green, G. M., Schlafly, E. F., Finkbeiner, D., et al. 2018, MNRAS, 478, 651
Haffert, S. Y., Bohn, A. J., de Boer, J., et al. 2019, NatAs, 3, 749
Hammond, I., Christiaens, V., Price, D. J., et al. 2023, MNRAS, 522, L51
Hoch, K. K. W., Rowland, M., Petrus, S., et al. 2025, Natur, 643, 938
Høg, E., Fabricius, C., Makarov, V. V., et al. 2000, A&A, 363, 385
Hom, E. F. Y., Marchis, F., Lee, T. K., et al. 2007, JOSAA, 24, 1580
Hunt, E. L., & Reffert, S. 2024, A&A, 686, A42
Indebetouw, R., Mathis, J. S., Babler, B. L., et al. 2005, ApJ, 619, 931
Janson, M., Gratton, R., Rodet, L., et al. 2021, Natur, 600, 231
Jeffries, R. D., Jackson, R. J., Wright, N. J., et al. 2023, MNRAS, 523, 802
Juillard, S., Christiaens, V., & Absil, O. 2022, A&A, 668, A125
Kanagawa, K. D., Muto, T., Tanaka, H., et al. 2016, PASJ, 68
Keppler, M., Benisty, M., Müller, A., et al. 2018, A&A, 617, A44
Kerr, R. M. P., Rizzuto, A. C., Kraus, A. L., & Offner, S. S. R. 2021, ApJ, 917, 23
Kostov, V. B., Orosz, J. A., Feinstein, A. D., et al. 2020, AJ, 159, 253
Kounkel, M., & Covey, K. 2019, AJ, 158, 122
Kroupa, P. 1995, MNRAS, 277, 1491
Kuhn, J. R., Potter, D., & Parise, B. 2001, ApJL, 553, L189
Lafrenière, D., Marois, C., Doyon, R., & Barman, T. 2009, ApJL, 694, L148
Lagrange, A. M., Gratadour, D., Chauvin, G., et al. 2009, A&A, 493, L21
Lanza, A. F., Flaccomio, E., Messina, S., et al. 2016, A&A, 592, A140
Long, M., Romanova, M. M., Kulkarni, A. K., & Donati, J.-F. 2011, MNRAS, 413, 1061
MacDonald, R. J., & Madhusudhan, N. 2017, MNRAS, 469, 1979
MacKay, D. J. C. 2003, Information Theory, Inference, and Learning Algorithms (Cambridge: Cambridge Univ. Press)
Magnani, L., Blitz, L., & Mundy, L. 1985, ApJ, 295, 402
Maire, A.-L., Langlois, M., Delorme, P., et al. 2021, JATIS, 7, 035004
Maire, A.-L., Langlois, M., Dohlen, K., et al. 2016, Proc. SPIE, 9908, 990834
Marois, C., Lafrenière, D., Doyon, R., Macintosh, B., & Nadeau, D. 2006, ApJ, 641, 556
Mesa, D., Keppler, M., Cantalloube, F., et al. 2019, A&A, 632, A25
Milli, J., Mouillet, D., Lagrange, A. M., et al. 2012, A&A, 545, A111
Monnier, J. D., Harries, T. J., Aarnio, A., et al. 2017, ApJ, 838, 20
Monnier, J. D., Harries, T. J., Bae, J., et al. 2019, ApJ, 872, 122
Müller, A., Keppler, M., Henning, T., et al. 2018, A&A, 617, L2
Oliphant, T. E. 2006, A Guide to NumPy, Vol 1 (USA: Trelgol Publishing)
Paardekooper, S.-J., & Mellema, G. 2006, A&A, 453, 1129
Park, S. J., Min, K. W., Seon, K. I., et al. 2012, ApJ, 754, 10
Paunzen, E., Netopil, M., Prišegen, M., & Faltová, N. 2024, A&A, 689, A270
Pinte, C., van der Plas, G., Ménard, F., et al. 2019, NatAs, 3, 1109
Pollack, J. B., Hubickyj, O., Bodenheimer, P., et al. 1996, Icar, 124, 62
Prato, L., & Simon, M. 2023, RNAAS, 7, 150
Qin, S., Zhong, J., Tang, T., & Chen, L. 2023, ApJS, 265, 12
Quanz, S. P., Avenhaus, H., Buenzli, E., et al. 2013, ApJL, 766, L2
Ruane, G., Ngo, H., Mawet, D., et al. 2019, AJ, 157, 118
Rustamkulov, Z., Sing, D. K., Mukherjee, S., et al. 2023, Natur, 614, 659
Sanghi, A., Xuan, J. W., Wang, J. J., et al. 2024, AJ, 168, 215
Schlafly, E. F., Finkbeiner, D. P., Schlegel, D. J., et al. 2010, ApJ, 725, 1175
Schlafly, E. F., Green, G., Finkbeiner, D. P., et al. 2014, ApJ, 786, 29
Schlegel, D. J., Finkbeiner, D. P., & Davis, M. 1998, ApJ, 500, 525

Shakura, N. I., & Sunyaev, R. A. 1976, MNRAS, 175, 613
Sigurdsson, S., Richer, H. B., Hansen, B. M., Stairs, I. H., & Thorsett, S. E. 2003, Sci, 301, 193
Smith, B. A., & Terrile, R. J. 1984, Sci, 226, 1421
Somers, G., Cao, L., & Pinsonneault, M. H. 2020, ApJ, 891, 29
Soummer, R., Pueyo, L., & Larkin, J. 2012, ApJL, 755, L28
Stapper, L. M., & Ginski, C. 2022, A&A, 668, A50
Stassun, K. G., Oelkers, R. J., Paegert, M., et al. 2019, AJ, 158, 138
Stolker, T., Bonse, M. J., Quanz, S. P., et al. 2019, A&A, 621, A59
Stolker, T., Marleau, G. D., Cugno, G., et al. 2020a, A&A, 644, A13
Stolker, T., Quanz, S. P., Todorov, K. O., et al. 2020b, A&A, 635, A182
Teague, R., Bae, J., Bergin, E. A., Birnstiel, T., & Foreman-Mackey, D. 2018, ApJL, 860, L12
Teague, R., Benisty, M., Facchini, S., et al. 2025, ApJL, 984, L6
Torres, C. A. O., Quast, G. R., da Silva, L., et al. 2006, A&A, 460, 695
Valegård, P. G., Ginski, C., Derkink, A., et al. 2024, A&A, 685, A54
van Boekel, R., Henning, T., Menu, J., et al. 2017, ApJ, 837, 132
van Capelleveen, R. F., Kenworthy, M. A., Ginski, C., et al. 2025, A&A, submitted
van Holstein, R. G., Girard, J. H., de Boer, J., et al. 2020, A&A, 633, A64
Virtanen, P., Gommers, R., Oliphant, T. E., et al. 2020, NatMe, 17, 261
Žerjal, M., Rains, A. D., Ireland, M. J., et al. 2021, MNRAS, 503, 938
Wahhaj, Z., Benisty, M., Ginski, C., et al. 2024, A&A, 687, A257
Wahhaj, Z., Milli, J., Romero, C., et al. 2021, A&A, 648, A26
Wang, J. J., Vigan, A., Lacour, S., et al. 2021, AJ, 161, 148
Watson, C. L., Henden, A. A., & Price, A. 2006, SASS, 25, 47
Weaver, G., Jeffries, R. D., & Jackson, R. J. 2024, MNRAS, 534, 2014
Xie, C., Choquet, E., Vigan, A., et al. 2022, A&A, 666, A32
Zari, E., Hashemi, H., Brown, A. G. A., Jardine, K., & de Zeeuw, P. T. 2018, A&A, 620, A172
Zhang, S., Zhu, Z., Huang, J., et al. 2018, ApJL, 869, L47
Zhang, Y., González Picos, D., de Regt, S., et al. 2024, AJ, 168, 246
Zhang, Y., Snellen, I. A. G., Bohn, A. J., et al. 2021, Natur, 595, 370
Zhang, Z., Liu, M. C., Claytor, Z. R., et al. 2021, ApJL, 916, L11